Coarse Versus Eddy-Permitting Global Ocean Simulations: Experiments With The UVic Earth System Climate Model

by

John Paul Gordon Spence

BSc, University of Victoria, 2000
MSc, University of Victoria, 2005

A Dissertation Submitted in Partial Fulfillment of the
Requirements for the Degree of

Doctor of Philosophy

in the School of Earth and Ocean Sciences

Coarse Versus Eddy-Permitting Global Ocean Simulations: Experiments With The UVic Earth System Climate Model

by

John Paul Gordon Spence

BSc, University of Victoria, 2000
MSc, University of Victoria, 2005

Supervisory Committee

Dr. A. J. Weaver, Supervisor (School of Earth and Ocean Sciences)

Dr. J. C. Fyfe, Member (School of Earth and Ocean Sciences)

Dr. A. H. Monahan, Member (School of Earth and Ocean Sciences)

Dr. O. A. Saenko, Member (School of Earth and Ocean Sciences)

Dr. F. W. Zwiers, Outside Member (Department of Mathematics)

Supervisory Committee

Dr. A. J. Weaver, Supervisor (School of Earth and Ocean Sciences)

Dr. J. C. Fyfe, Member (School of Earth and Ocean Sciences)

Dr. A. H. Monahan, Member (School of Earth and Ocean Sciences)

Dr. O. A. Saenko, Member (School of Earth and Ocean Sciences)

Dr. F. W. Zwiers, Outside Member (Department of Mathematics)

Abstract

This dissertation presents experiments with the UVic Earth System Climate Model that explore the sensitivity of global climate simulations to an increase of horizontal resolution into the ocean eddy-permitting range. Model versions, with resolutions ranging from 1.8° (latitude) ×3.6° (longitude) to 0.2°×0.4°, are evaluated in control states and in response to climate perturbations. The effect of resolution on ocean volume transport, ocean heat transport, water mass formation, and sea ice distribution are investigated within the framework of three foci: 1) the Atlantic meridional overturning circulation and its response to surface freshwater forcing; 2) the Southern Ocean overturning circulation and its response to poleward intensifying winds concomitant with increasing atmospheric CO_2; 3) the Southern Ocean temperature and Antarctic Circumpolar Current response to poleward intensifying winds alone.

These sensitivity studies shed light on the ability to draw firm conclusions from coarse resolution modelling results.

First, it is found that the simulation of western boundary currents, sea ice and meridional heat transport in the North Atlantic Ocean are improved with increasing resolution. A slowdown of the Atlantic meridional overturning circulation is robustly produced at both coarse and ocean eddy-permitting resolutions in response to freshwater forcing applied evenly over the Labrador Sea and exclusively along its western boundary. An evaluation of the forcing impact on different regions of NADW formation with tracers reveals that increased Labrador Sea deep convection at higher resolution may mitigate the influence of better resolved boundary current transport. With increasing resolution there is less cooling in the subpolar west Atlantic, more cooling in the subpolar east Atlantic, and greater variability in the deep ocean response to the western boundary forcing.

Second, it is found that as resolution increases the interior ocean circulation becomes more adiabatic, with deep water formed in the North Atlantic tending to upwell more in the Southern Ocean and less in the low-latitude oceans. For some density classes the transformation rate derived from surface buoyancy fluxes can provide a proxy for the net meridional transport in the upper Southern Ocean. The response of the Southern Ocean overturning to poleward intensifying southern hemisphere winds concomitant with increasing atmospheric CO_2 suggest that the circulation associated with the formation of Antarctic Intermediate Water is likely to strengthen through the 21^{st} century.

Third, the zonal mean structure of the Southern Ocean temperature response to poleward intensifying winds through the 21^{st} century, with warming between 40-55°S and cooling at higher and lower latitudes, remains robust as model resolution increases. However, the migration of distinct ocean fronts at finer resolutions can produce a strong local intensification of the temperature response. There is also

less high latitude cooling and a greater loss of sea ice thickness at eddy-permitting resolutions, in conjunction with a significant increase in southward ocean eddy heat transport. Antarctic Circumpolar Current transport is found to increase in response to the forcing at both coarse and eddy-permitting resolutions.

Table of Contents

List of Tables

List of Figures

Acknowledgements

I wish to extend my sincere thanks to my supervisor, Andrew Weaver, for his superior guidance and leadership. I am very grateful for the kind mentorship provided by my committee members: John Fyfe, Richard Karsten, Adam Monahan, Oleg Saenko, and Francis Zwiers. Special thanks to Michael Eby, Wanda Lewis, Katrin Meissner, Alvaro Montenegro, Ed Wiebe and the rest of the climate lab for providing a wonderful learning environment. I feel blessed to have worked with you all.

I am very grateful to my family for their endless support and encouragement; my deep gratitude to Roberta and Paul Harris, Michael Burlington (in memory), John (in memory), Joan, Holly and Tom Spence, Sean, Lucy, Elliot, and Phoebe Spence, Gordon (in memory) and Alice Stevens, Tom (in memory) and Winnifred Burlington, as well as Jack (in memory) and Norma (in memory) Spence.

This research was supported by the National Science and Engineering Research Council, the Canadian Foundation for Climate and Atmospheric Studies and the Canadian Climate Variability Research Network.

Chapter 1

Introduction

1.1 Purpose of Dissertation

The search for an understanding of climate change, both past and future, has lead to the development of complex General Circulation Models (GCMs). Computational constraints have limited the vast majority of centurial time-scale global GCM simulations to coarse horizontal resolutions (i.e. $> 1°$). These simulations only capture the large-scale features of the ocean circulation, and are obliged to parametrize the effects of the unresolved motions. Consider that most of the observed ocean kinetic energy occurs on the mesoscale, with length scales of 10 to 100 km (*Ducet et al.* 2000, *Wunsch* 2007). The Intergovernmental Panel on Climate Change (IPCC) Third Assessment Report (TAR) noted considerable debate regarding the adequacy of coarse horizontal resolution ocean models and warned that some results at $> 1°$ resolution should be treated cautiously (*McAvaney et al.* 2001). The TAR further identified a lack of systematic experiments exploring model sensitivities to increasing resolution as restricting the ability to draw firm conclusions from GCMs. This dissertation focuses on the Atlantic Ocean and the Southern Ocean, where the simulation of a number of important ocean processes are known, or suspected to be sensitive to horizontal resolution.

The meridional overturning circulation (MOC) of the Atlantic Ocean is respon-

sible for the majority of poleward ocean heat transport in the northern hemisphere (*Hall and Byrden* 1982). Regional modelling studies have demonstrated a dependence of Atlantic heat transport on resolution, with coarse resolution models often simulating significantly less northward transport than observed (*Fanning and Weaver* 1997, *Bryan and Smith* 1998). This deficiency has been partially attributed to the generally poor resolution of western boundary currents and difficulties in properly positioning the North Atlantic Current (*Beckmann et al.* 1994, *Treguier et al.* 2005). Insufficient poleward ocean heat transport is attributed to excessive North Atlantic sea ice coverage (*Weaver et al.* 2001). Coarse resolution models have also been criticized for inaccuracies in their simulation of North Atlantic Deep Water (NADW) formation (*Wood et al.* 1999). Highly localized processes such as interior diapycnal mixing (*Polzin et al.* 1997) and convection (*Canuto et al.* 2004), both of which play critical roles in deepwater formation and the MOC, are likely sensitive to model resolution. *Roberts et al.* (2004) found a less pronounced weakening of the Atlantic MOC and heat transport in response increasing atmospheric CO_2 when the ocean resolution of their climate model was increased from 1° to 0.33°.

The Southern Ocean is a primary conduit for the interbasin exchange of oceanic properties, and the majority of ocean water masses are either formed, modified, or transit through the region (*Macdonald and Wunsch* 1996). Observational evidence suggests that standing and transient eddies induce significant meridional transport in the Southern Ocean (*Sloyan and Rintoul* 2001), leaving a particular need to parametrize their effects in coarse resolution models (*Gent and McWilliams* 1990). Circulations induced by eddy parametrizations can have strong cross-isopycnal flows in coarse-resolution models (e.g., *Hirst and McDougall* (1998)), but it is unclear if these circulations accurately track the transport pathways induced by resolved eddies. Regional modelling studies have demonstrated that the overall dense-to-light conversion of Southern Ocean water depends on whether eddies are parametrized

or permitted (*Hallberg and Gnanadesikan* 2006). Furthermore, the degree of connection between the MOC of the Southern Ocean and that of the Atlantic Ocean has been shown to be sensitive to differing parametrizations of mesoscale tracer transport (*Danabasoglu et al.* 1994). The ability of coarse-resolution models employing mesoscale eddy parametrization schemes to accurately capture the influence of Southern Ocean wind stress forcing has also been questioned (*Meredith and Hogg* 2006, *Böning et al.* 2008). Coarse resolution models also poorly resolve the distinct frontal structures of the Southern Ocean and under-represent bathymetry features that guide the path of the Antarctic Circumpolar (ACC) (*Sallee et al.* 2008).

All of the factors discussed above have the potential to produce substantial differences between simulations of the ocean circulation by coarse and high resolution models. However, the use of high resolution models has generally been limited by computational constraints requiring non-global spatial domains with idealized boundary conditions and short integration periods (e.g. *Oschlies* (2002), *Hallberg and Gnanadesikan* (2006), *Screen et al.* (2008)). Significant uncertainties remain regarding the effects of reducing the influence of parametrizations in ocean simulations in favour of resolved advection. The IPCC again noted the lack of a comprehensive suite of high resolution global climate integrations in their Fourth Assessment Report (*Randall et al.* 2007).

This dissertation primarily focuses on the effect of resolution on the ocean circulation, which leads one to question whether a coupled climate model is required, or if an ocean only model would be sufficient. Several uncoupled ocean model studies have evaluated the effects of increasing resolution into the ocean eddy-permitting range (e.g. *The FRAM Group (D. Webb et al.)* (1991), *Hallberg and Gnanadesikan* (2006)). However, ocean only models exhibit serious shortcomings in the conceptual formulation of surface buoyancy fluxes. Ocean only models are forced to specify surface heat and freshwater fluxes, usually based on restoring boundary conditions for tem-

perature and salinity. In doing so they assume an infinite heat capacity atmosphere and that the surface freshwater flux at a given place depends on the local sea surface salinity; both of these assumptions are clearly incorrect. Uncoupled ocean models also do not allow for hydrological and thermodynamic processes in other climate components (e.g. atmosphere and sea ice) to feedback on the ocean. Furthermore, relatively small changes in the freshwater or heat exchange between the ocean and atmosphere may produce dramatic changes in the ocean circulation, with impacts on the global climate (*Weaver and Hughes* 1992). Using a coupled climate model allows heat and fresh water to be properly conserved, and fluxes between the ocean, atmosphere and sea ice components can dynamically respond to each other.

The purpose of this dissertation is to address the need for systematic experiments exploring the impacts of increasing horizontal resolution in GCMs. A series of centurial time-scale global simulations, with horizontal resolutions ranging from coarse to ocean eddy-permitting, are evaluated in both control states and in response to climate perturbation forcings. Aside from the eddy-permitting simulation based on the global climate model developed at the Hadley Centre for Climate Prediction and Research, which is configured to have a resolution of $1/3^\circ$ in its oceanic component (*Roberts et al.* 2004), the simulations presented herein are the longest integrated ocean eddy-permitting global climate simulations currently available.

1.2 Outline of Dissertation

The next chapter (Chapter 2) describes the climate model used in this study, focusing on the ocean, atmosphere, sea ice, and land surface components. Details regarding the methodology used to increase the horizontal resolution of the model are provided in the experimental design sections of subsequent chapters.

A weakened MOC in response to surface freshwater forcing at NADW formation sites is commonly evoked as a mechanism to explain large-scale climate events found

in paleorecords. Chapter 3 begins by evaluating the sensitivity of a control state North Atlantic climate to increasing horizontal resolution. This is followed by an evaluation of model responses to freshwater forcing scenarios that simulate a massive drainage of proglacial lakes Agassiz and Ojibway into the Labrador Sea (commonly referred to as the 8.2 kyr event). Freshwater forcing is applied both over the entire Labrador Sea and exclusively along its western boundary.

Chapter 4 focuses on the resolution dependence of the MOC in the Southern Ocean. Both time-mean and transient overturning circulations are evaluated. The pre-industrial control state of the MOC, and its response to an observed and projected poleward shift and strengthening of southern hemisphere westerly winds concomitant with increasing atmospheric CO_2 through the 20^{th} and 20^{st} centuries are examined. An attempt is also made to connect the strength of the MOC to the local buoyancy input at the surface.

Observations over the past few decades reveal that parts of the Southern Ocean have been warming at nearly twice the rate of the global ocean. Coarse resolution models indicate a link between the forementioned poleward intensifying winds and the enhanced Southern Ocean warming. Coarse resolution models also suggest a significant increase in the volume transport of the ACC in response to the wind forcing. However, given the importance of mesoscale structures and motions in the Southern Ocean, the accuracy of these model results are strongly debated. Chapter 5 examines the horizontal resolution dependence of the Southern Ocean temperature and ACC transport response to poleward intensifying winds through the 20^{th} and 21^{st} centuries. Chapter 6 concludes this dissertation by consolidating all results and highlighting the key contributions.

Chapter 2

Model Description

2.1 The Coupled Climate Model

This dissertation employs version 2.7 of the intermediate complexity University of Victoria Earth System Climate Model (UVic ESCM). It couples a three-dimensional ocean general circulation model, a two-dimensional atmospheric model, a thermodynamic/dynamic sea ice model and a simple land surface model. The UVic ESCM has a global domain and model components share the same horizontal grid resolution. It is forced from start-up to a control state by variations in insolation and surface winds. The model has been validated against present-day climatology (*Weaver et al.* 2001) and various proxy paleo-reconstructions (e.g. *Meissner et al.* (2003)). Its computational efficiency and ability to maintain a stable climate without explicit flux adjustments permits a wide range of parameter sensitivity studies over long timescales (e.g. *Wiebe and Weaver* (1999)). Below is a description of the ocean component, followed by more brief descriptions of the atmosphere, sea ice, and land surface components (for a more complete description see *Weaver et al.* (2001)).

2.1.1 The Ocean Component

The ocean component is the Geophysical Fluid Dynamics Laboratory Modular Ocean Model (MOM) version 2.2 (*Pacanowski* 1995). The employed version of MOM is

subject to the Boussinesq and hydrostatic approximations. It has 19 vertical levels that increase parabolically in thickness from 50m at the surface to 518m at depth. The ocean model conserves volume, and surface freshwater fluxes are converted to fluxes of salt with a constant salt-to-freshwater mass ratio of 3.49×10^{-2}.

The Principal Equations

The longitude (λ), latitude (ϕ), and vertical (z) components of velocity ($\mathbf{v}$) are u, v, and w, respectively. Under the Boussinesq approximation, the equation for the conservation of mass becomes

$$\nabla \cdot \mathbf{v} = 0, \tag{2.1}$$

and the local density (ρ) is replaced by a constant reference density ($\rho_0 = 1035\ kgm^{-3}$) except when coupled to gravitational acceleration in the vertical momentum equation. Under the hydrostatic approximation

$$\frac{\partial p}{\partial z} = -g\rho, \tag{2.2}$$

where g is the gravitational acceleration, the vertical component of the momentum equation is diagnosed from the continuity equation (Eq. 2.1). Constant eddy viscosity coefficients are used in both the horizontal (A_M) and vertical ($\kappa_M = 1 \times 10^{-3}\ m^2 s^{-1}$) directions. A_M is chosen based on the horizontal resolution of each simulation, and is discussed extensively in the following chapters (see also Appendix A). The horizontal component of the momentum equation can be written as

$$\frac{D\mathbf{v}_h}{Dt} + f(\mathbf{k} \times \mathbf{v})_h = -\frac{1}{\rho_0}\nabla_h p + \nabla_h \cdot (A_m \nabla_h \mathbf{v}_h) + \frac{\partial}{\partial z}(\kappa_M \frac{\partial \mathbf{v}_h}{\partial z}), \tag{2.3}$$

where $\mathbf{v}_h = (u, v)$ is the horizontal velocity, f is the Coriolis parameter, p is the pressure, ∇_h is a two-dimensional horizontal gradient operator, and

$$\frac{D}{Dt} = \frac{\partial}{\partial t} + \mathbf{v}_h \cdot \nabla_h + \frac{\partial w}{\partial z}. \tag{2.4}$$

The boundary conditions for momentum at the surface ($z = 0$) are

$$w = 0, \tag{2.5}$$

and

$$\rho_0 A_M \frac{\partial \mathbf{v}_h}{\partial z} = \boldsymbol{\tau}_a, \tag{2.6}$$

where $\boldsymbol{\tau}_a$ is the horizontal wind stress vector at the surface. The boundary conditions for momentum at the bottom ($z = -H$) are

$$w = 0, \tag{2.7}$$

and

$$\rho_0 A_M \frac{\partial \mathbf{v}_h}{\partial z} = \boldsymbol{\tau}_b, \tag{2.8}$$

where $\boldsymbol{\tau}_b$ is the exerted bottom stress vector calculated from

$$\boldsymbol{\tau}_b = \rho_0 C_{DB} |\mathbf{v}_h| \mathbf{v}_h, \tag{2.9}$$

where $C_{DB} = 1.3 \times 10^{-3}$ is a dimensionless drag coefficient. The boundary conditions for momentum at sidewalls are

$$\mathbf{v}_h \cdot \mathbf{n} = 0, \tag{2.10}$$

and

$$\mathbf{v}_h \cdot \mathbf{t} = 0, \tag{2.11}$$

where $\mathbf{n}$ and $\mathbf{t}$ are unit vectors normal and tangent to sidewalls (no-slip boundary condition).

The ocean model separates the high velocity barotropic dynamics from the slower baroclinic dynamics. Barotropic momentum equations are solved by the implicit free-surface formulation of *Dukowicz and Smith* (1994). This approach applies numerical damping to suppress fast barotropic waves, allowing the models barotropic time step to equal the baroclinic time step, and necessitates a constant volume ocean.

The ocean has a strong tendency to diffuse tracers along directions of constant potential density, rather than constant depth. For this reason, isopycnal diffusion of tracers, rather than horizontal diffusion, is used to parametrize subgrid-scale mixing. Mixing of tracers associated with mesoscale eddies is also parametrized according to *Gent and McWilliams* (1990) (hereafter referred to as GM90). In low-stratification regions the GM90 slopes and tracer fluxes are tapered according to the scheme of *Gerdes et al.* (1991). The conservation equations for active tracers of potential temperature (θ) and salinity (s) can be expressed as

$$\begin{aligned}\frac{D\theta}{Dt} &= \nabla_h \cdot \{A_{ISO}\nabla_h\theta) + (A_{ISO} - A_{ITH})\mathbf{S}\frac{\partial\theta}{\partial z}\} \\ &+\frac{\partial}{\partial z}\{(A_{ISO} + A_{ITH})\mathbf{S}\cdot\nabla_h\theta + (\kappa_z + A_{ISO}S^2)\frac{\partial\theta}{\partial z}\},\end{aligned} \tag{2.12}$$

and

$$\begin{aligned}\frac{Ds}{Dt} &= \nabla_h \cdot \{A_{ISO}\nabla_h s) + (A_{ISO} - A_{ITH})\mathbf{S}\frac{\partial s}{\partial z}\} \\ &+\frac{\partial}{\partial z}\{(A_{ISO} + A_{ITH})\mathbf{S}\cdot\nabla_h s + (\kappa_z + A_{ISO}S^2)\frac{\partial s}{\partial z}\},\end{aligned} \tag{2.13}$$

where

$$\mathbf{S} = -\frac{\nabla_h\rho}{\frac{\partial\rho}{\partial z}}, \tag{2.14}$$

is the isopycnal slope vector with magnitude S (see *Pacanowski and Griffies* (2000)

sections 4.2.1 and 4.2.4). The isopycnal diffusivity coefficient (A_{ISO}) and the GM90 isopycnal thickness diffusion coefficient (A_{ITH}) are modified according to the model horizontal resolution (discussed in following chapters). Setting $A_{ISO} = A_{ITH}$ is common (*Pacanowski* 1995). In low-stratification regions the GM90 slopes and tracer fluxes are tapered according to the scheme of *Gerdes et al.* (1991). The vertical diffusivity (κ_z) ranges from 3.0×10^{-5} m^2s^{-1} near the surface to 1.3×10^{-4} m^2s^{-1} at depth according to the scheme of *Bryan and Lewis* (1979). Convective mixing of tracers is parametrized by an explicit full convection scheme, wherein statically unstable cells in a water column are explicitly mixed together to completely remove all instabilities each time step.

The net heat Q_H and implied salinity Q_S fluxes into the ocean are

$$Q_H = (1 - A_i)Q_{to} + A_i Q_b \tag{2.15}$$

$$Q_S = \rho_0 S^* \{E - P - R + \frac{Q_b - Q_t}{\rho_0 L_f}\} \tag{2.16}$$

where $S^* = 34.9$ psu is a representative salinity for the ocean and R is the runoff from land. A_i, Q_{to}, Q_b, Q_t and L_f are given by Eqs. 2.20 and 2.21, whereas E and P are given by Eq. 2.19.

The density of sea water is a non linear function of potential temperature, salinity and pressure that is calculated from empirical formula and can be simply expressed as

$$\rho = \rho(\theta, s, p). \tag{2.17}$$

The time-evolving ocean circulation is governed by seven principal equations (Eq. 2.1, Eq. 2.2, Eq. 2.3, Eq. 2.12, Eq. 2.13, Eq. 2.17; note that Eq. 2.3 is equivalent

to two scalar equations) , which contain seven unknown variables (ρ, u, v, w, θ, S, and p).

2.1.2 The Atmosphere Component

The atmosphere component of the UVic ESCM is based on the two-dimensional energy-moisture balance model of *Fanning and Weaver* (1996). Wind fields are not calculated by the model, but are specified from the longterm monthly mean climatology of the NCEP50 reanalysis (*Kistler et al.* 2001) for computational efficiency. The model resolves the annual cycle, and the incoming solar radiation at the top of the atmosphere depends on orbital parameters. Cloud radiative feedbacks are not included. Sea level air temperature (T_a) and specific humidity (q_a) are the two prognostic variables. The vertically integrated thermodynamic energy and moisture balance equations assume an exponentially decreasing vertical distribution of energy and specific humidity.

The vertically integrated thermodynamic energy equation can be expressed as

$$\rho_a h_t c_{pa} \frac{\partial T_a}{\partial t} = Q_{HT} + C_a Q_{SW} + Q_{LH} + Q_{LW} + Q_{SH} - Q_{PLW}, \tag{2.18}$$

where ρ_a is the air density, $h_t = 8.4\ km$ is a constant scale height for thermal energy, and $c_{pa} = 1004\ Jkg^{-1}K^{-1}$ is the specific heat capacity of air at constant pressure. Terms on the right hand side of Eq. 2.18 represent sources and sinks of atmospheric heat: Q_{HT} is the heat transport parametrized by Fickian diffusion; Q_{SW} is the incoming shortwave at the top of the atmosphere, with a $C_a = 0.3$ absorption coefficient to parametrized atmospheric absorption; Q_{LH} is the latent heat flux into the atmosphere; Q_{LW} is the net upward longwave radiative flux into the atmosphere; Q_{SH} is the sensible heat flux calculated from bulk formula; Q_{PLW} is the outgoing planetary longwave radiation that parametrizes water vapour feedbacks and the radiative forcing associated with changes in atmospheric CO_2.

The vertically integrated moisture balance equation can be expressed as

$$\rho_a h_q \{\frac{\partial q_a}{\partial t} - \nabla \cdot (\kappa \nabla q_a) + \beta \nabla \cdot (\mathbf{v} q_a)\} = \rho_o (E - P), \tag{2.19}$$

where $h_q = 1.8\ km$ is a constant scale height for specific humidity, q_a is the surface specific humidity, κ is an eddy diffusivity, $\beta = 0.4$ relates the vertically averaged advective moisture transport to the surface advective transport, $\mathbf{v}$ is the vertically averaged wind, E is evapouration or sublimation calculated from bulk formula, and P is precipitation that occurs in the form of rain or snow when the relative humidity exceeds 90%.

2.1.3 The Sea Ice Component

The sea ice model incorporates energy conserving ice-snow thermodynamics (*Hibler* 1979) and an elastic-viscous-plastic rheology (*Hunke and Dukowicz* 1997). Sea ice has no heat capacity and the surface temperature is in instantaneous balance with the external forcing. The model predicts ice thickness (H_i), areal fraction (A_i) and ice surface temperature (T_i).

The change in ice thickness over a grid cell is given by

$$\frac{\partial H_i}{\partial t} = \frac{(Q_b - Q_t)}{\rho_i L_f} - \frac{\rho_o}{\rho_i} E - L(H_i), \tag{2.20}$$

where Q_b is the heat flux from the ocean, Q_t is the heat flux from the atmosphere (both are positive downward); $\rho_i = 913\ \text{kgm}^{-3}$ and $\rho_o = 1035\ \text{kgm}^{-3}$ are density values for ice and water, respectively and $L_f = 3.34 \times 10^5\ \text{Jkg}^{-1}$ is the latent heat of fusion of ice. E is the sublimation rate and $L(H_i)$ is the horizontal advection of H_i. Grid cells are allowed to contain both ocean and sea ice, and the total heat flux from the atmosphere is calculated for both the open water (Q_{to}) and ice covered (Q_{ti}) portions.

The change in ice areal fraction depends on the growth rates over ice-covered and open water areas as prescribed by

$$\begin{aligned}\frac{\partial A_i}{\partial t} = & \begin{cases} \frac{(1-A_i)}{H_0}\frac{(Q_b-Q_{to})}{\rho_i L_f} & \text{if } Q_{to} < Q_b \\ 0 & \text{otherwise} \end{cases} \\ + & \begin{cases} \frac{A_i}{2H_i}(\frac{(Q_b-Q_t)}{\rho_i L_f} - \frac{\rho_o}{\rho_i}E) & \text{if } Q_t > Q_b \\ 0 & \text{otherwise} \end{cases} \\ - & L(A_i), \end{aligned} \tag{2.21}$$

where $H_0 = 0.01$ m is a demarcation thickness between thick and thin ice. The first term on the right hand side of Eq. 2.21 parametrizes the change in area under freezing conditions, where the open water portion $(1 - A_i)$ exponentially decays with time constant $H_0\rho_i L_f/(Q_b - Q_{to})$. The second term parametrizes melting and assumes that all ice is uniformly distributed in thickness between 0 and $2H_i/A_i$. Assuming uniform melting over time $\triangle t$, this term opens up area where thickness is less than $-(\frac{(Q_b-Q_t)}{\rho_i L_f} - E)\triangle t$.

The surface temperature is calculated by equating the conductive flux through the ice (and snow) with the energy flux at the surface:

$$\frac{T_i - T_f}{\frac{H_i}{I_{cond}} + \frac{H_s}{S_{cond}}} = Q_{ti}(T_i), \tag{2.22}$$

where $I_{cond} = 2.166$ $\mathrm{Wm^{-1}K^{-1}}$ is a constant ice conductivity (and H_s and $S_{cond} = 0.31$ $\mathrm{Wm^{-1}K^{-1}}$ are the thickness and conductivity of snow respectively). The maximum value of T_i is limited to the freezing temperature.

The momentum balance for sea ice dynamics is expressed as

$$m\frac{\partial \mathbf{v}}{\partial t} = \nabla \cdot \sigma - mf\mathbf{k} \times \mathbf{v} + \boldsymbol{\tau}_a + \boldsymbol{\tau}_w - mg\nabla H, \tag{2.23}$$

where $\mathbf{v}$ is the ice velocity, σ is the elastic-viscous-plastic internal stress tensor, f is the Coriolis parameter, $\mathbf{k}$ is the unit normal vector in the vertical, $\boldsymbol{\tau}_a$ and $\boldsymbol{\tau}_w$ are the atmospheric (wind) and oceanic stresses, H is the sea surface dynamic height, m is the ice mass per unit area, and $g = 9.81$ ms^{-2} is the acceleration due to gravity.

2.1.4 Land Surface Component

Precipitation on land is treated by a simple bucket model, detailed by *Matthews et al.* (2003). Inputs to the bucket are rain and snowmelt; outputs are evapouration and river runoff. Runoff occurs when a grid cell's 15 cm deep bucket overflows, and it is returned to the ocean via weighted river discharge points. The parametrization of evapouration on land includes a surface resistance. Surface resistance decreases as a bucket fills and is dependent on vegetation type. One of seven vegetation types are statically assigned to each grid cell. The vegetation type also determines the land surface albedo in the absence of snow.

Chapter 3

The Atlantic Meridional Overturning Circulation: Sensitivity to Freshwater Forcing

3.1 Introduction

Variations in the poleward transport of heat by the Atlantic meridional overturning circulation (AMOC) is commonly evoked as a mechanism to explain large-scale climate events found in paleorecords (*Bond et al.* 1993, *Rahmstorf* 2002). A wide range of modeling studies have demonstrated a weakened AMOC in response to surface freshwater forcing at NADW formation sites (e.g. *Stommel* (1961), *Weaver and Hughes* (1992), *Stouffer et al.* (2006)): an increased freshwater flux creates more stably stratified surface water, which reduces deep water formation and its concomitant meridional heat transport, producing a cooling of northern hemisphere climate. Of the few studies that have systematically examined the effects of increasing model resolution, none evaluated differences in the response to deep water formation perturbations. Earlier research focused on ocean volume and heat transports at (or near) equilibrium with model domains limited to the Atlantic basin (e.g. *Bryan* (1991), *Beckmann et al.* (1994), *Böning et al.* (1996), *Fanning and Weaver* (1997, 1998),

Smith et al. (2000), *Oschlies* (2002)). *Duffy et al.* (2002) evaluated the unperturbed state in a set of global Earth System Models of Intermediate Complexity (EMICs), but the finest resolution model was 1°× 1°. This experiment evaluates model states before and after applying freshwater forcing similar to the 8.2 kyr event.

The 8.2 kyr event refers to the widespread cooling found in paleoclimate records in Greenland, Europe, North America and the tropical Atlantic roughly 8,200 calendar years ago (*Alley and Agustsdottir* 2005, *Morrill and Jacobsen* 2005). The forcing for this event is thought to be the catastrophic final drainage of proglacial lakes Agassiz and Ojibway (hereafter simply referred to as Lake Agassiz) into Hudson Bay and the Labrador Sea (*Barber et al.* 1999). Paleoevidence suggests that roughly 1.65×10^{14} m^3 of freshwater drained in less than a year (equivalent to twice the volume of the present day Caspian Sea) creating one of the largest abrupt climate events of the Holocene (*Leverington et al.* 2002, *Clarke et al.* 2003).

The deep ocean requires centuries-to-millennia to reach a thermodynamic equilibrium (*Broecker* 1991). In this study, the equilibration of high resolution models are advanced by initiating them from an interpolated equilibrium state of a coarse resolution version of the UVic ESCM. Models with horizontal resolutions of 0.6° (latitude) ×1.2° (longitude), 0.3°×0.6° and 0.2°×0.4° are further integrated from the 3000 year state of a 1.8°× 3.6° model. The two highest resolution models have grid spacings finer than typical ocean eddy wavelengths (100-200 km) (*Stammer* 1997), but coarser than the first baroclinic Rossby radius of deformation at high latitudes (*Smith et al.* 2000, *Oschlies* 2002), which qualifies them as eddy-permitting. All models are integrated under orbital, atmospheric (CO_2 = 280 ppm) and land surface conditions corresponding to the year 1850, rather than 8.2 kyr conditions (CO_2 = 260 ppm). The exclusion of many forcings specific to the 8.2 kyr event limits a detailed comparison to proxy evidence.

Two freshwater perturbation scenarios are investigated at each model resolution.

The first follows previous modeling studies (e.g. *Renssen et al.* (2001), *Bauer et al.* (2004), *Wang and Mysak* (2005)) by distributing the freshwater uniformly over the entire Labrador Sea. However, most of the transport of the North Atlantic subpolar gyre occurs in coastal boundary currents and it is likely that much of the freshwater discharged by the 8.2 kyr event would have initially been confined to the continental margin (*Wunsch* 2006). The ability of boundary currents to influence the AMOC response is investigated in the second scenario, wherein the freshwater is applied along the coastline of north-east North America. The working hypothesis was that stronger boundary currents in higher resolution models may influence the the response of the AMOC, local convective activity and climate to freshwater forcing (*Saenko et al.* 2007a). The purpose of this study is to determine if the coarse resolution AMOC response remains robust at finer horizontal resolutions.

The outline of the remainder of this chapter is as follows: Section 3.2 describes the experimental design. Section 3.3 evaluates model states prior to forcing and section 3.4 examines the response to 8.2 kyr event freshwater forcing scenarios. Conclusions are presented in section 3.5.

3.2 Experimental Design

All UVic ESCM simulations in this study are integrated under pre-industrial (year 1850) orbital, atmospheric and land surface conditions. Table 3.1 lists the values of the primary parameters modified in each simulation as well as their pre-forcing integration times. Following the resolution criterion of *Bryan et al.* (1975) (see also Appendix A), the horizontal mixing coefficient for momentum is reduced by roughly the factor increase in resolution (isopycnal tracer mixing coefficients were similarly reduced). The number of vertical ocean levels is held fixed and the bathymetry is left unchanged with resolution. For example, $0.6° \times 1.2°$ bathymetry is constructed by dividing each cell in the $1.8° \times 3.6°$ bathymetry matrix into a 3×3 matrix. This tech-

Table 3.1: Horizontal resolution parameters and salient features of North Atlantic forcing simulations

Horizontal Resolution	1.8°×3.6°	0.6°×1.2°	0.3°×0.6°	0.2°×0.4°
A_M ($\times 10^8 cm^2/s$)	20	7	3	1.5
A_{ISO} and A_{ITH} ($\times 10^6 cm^2/s$)	4	1.5	1	0.75
Control Integ. Length (years)	3000	450	100	50
Model Speed (years/day)	300	20	1.25	0.5
Subtropical Transport (Sv)	44.3	48.9	52.9	49.1
Gulf Stream Curr. Spd. (cm/s)	23.4	38.7	47.4	52.1
Subpolar Transport (Sv)	-25.9	-24.4	-27.9	-27.2
Labrador Curr. Spd. (cm/s)	3.5	11.2	13.3	17.4
Total Conv. Energy ($\times 10^{17} J$)	9.2	9.2	7.8	7.7
Lab. Conv. Energy ($\times 10^{16} J$)	0.6	10.5	8.4	5.2
(Lab. Conv.*100)/Total	0.7%	11.4%	10.8%	6.8%

A_M, A_{ISO} and A_{ITH} are the horizontal viscosity, isopycnal diffusion and isopycnal thickness diffusion coefficients, respectively. All models are run on an upgraded NEC-SX6 supercomputer. Subtropical and subpolar transport refers to the maximum barotropic transport found within the gyres. The Gulf Stream and Labrador current speeds are the maximum near-surface speeds located within 2° wide meridional bands centered along 68° W and 55° W, respectively. Total potential energy released by ocean convection was calculated from grid cells with a ventilation depth >300 m over the months of January, February and March in the last year of the control runs.

nique allows us to focus on the resolution of ocean boundary currents and boundary layer freshwater flux forcing, while excluding both the attributes and complications arising from flows through regions of complex bathymetry. The horizontal resolution of the land, atmosphere and sea ice components are also increased in the same manner as the bathymetry. All experiments use the same values for vertical ocean mixing coefficients.

The integration times of the two eddy-permitting models are not sufficient to remove all the long timescale transients in the deep ocean. Timestep interval data does not show a consistent linear trend in global mean ocean potential temperature,

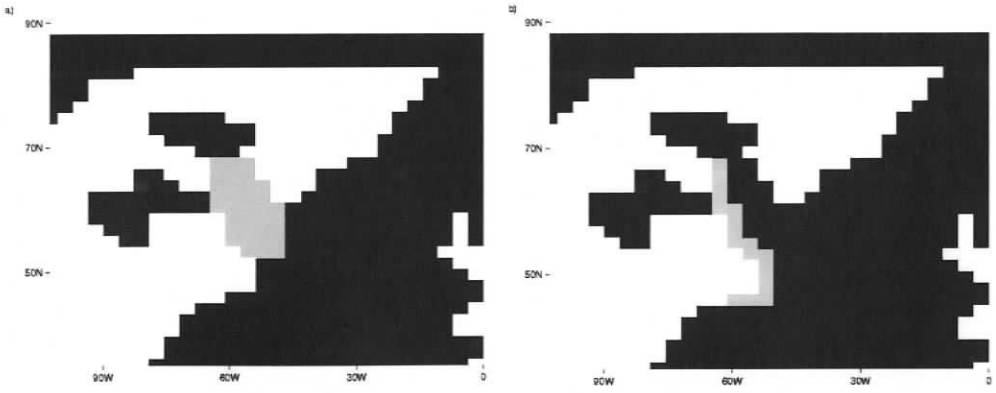

Figure 3.1: In the LAB forcing scenario, the freshwater was distributed over the grey region shown in (a), the size of which is independent of horizontal resolution. In the BC forcing scenario, the freshwater was applied to a one grid cell wide coastal strip in the $1.8° \times 3.6°$ model (b), and in a two grid cell wide coastal strip in the higher resolution models (not shown).

but a weak linear salinity trend of roughly 0.0040 psu/century is evident in the three higher resolution models. By the end of the control equilibrations the range of global mean ocean potential temperature and salinity among the models is 3.63 K to 3.65 K and 34.79 psu to 34.81 psu, respectively.

The 8.2 kyr event is simulated by adding 1.65×10^{14} m^3 of freshwater to the surface of the Labrador Sea. To prevent the converted salt flux from generating negative salinity values freshwater is applied at a rate of 1.75 Sv ($Sv \equiv 10^6$ m^3/s) for a period of 3 years. Two perturbation scenarios were carried out for each control run. In the first scenario (hereafter referred to as LAB forcing), the freshwater was distributed uniformly over the entire Labrador Sea (Fig. 3.1a). In the second scenario (hereafter referred to as BC forcing), the freshwater was applied as close to the coastline of northeastern North America as possible (Fig. 3.1b). For the $1.8° \times 3.6°$ model, shown in frame (b), the boundary forcing region was one grid box wide. For the three higher resolution models the boundary forcing region was two grid boxes wide.

3.3 Evaluation of Control Climate

3.3.1 North Atlantic Barotropic Circulation

Since the topography and applied wind stress curl is the same in each model, linear Sverdrup theory predicts equivalent barotropic ocean volume transports. Pronounced differences should occur in the North Atlantic subpolar gyre as well as the western boundary of the subtropical gyre where the local dynamics are non-linear and significantly influenced by deep water flows (*Bryan et al.* 1995).

Figure 3.2 shows the annual mean North Atlantic barotropic stream function for the last year of the control runs at each resolution. In the subtropical gyre, the simulations follow Sverdrup theory as similar transports are produced in the eastern half of the gyre, while differences dominate near the western boundary. The width of the western boundary transport is more realistically represented at higher resolution; it is considerably narrowed and restricted to the edge of the continental shelf. The maximum barotropic transport within the subtropical gyre (Table 3.1) in these simulations compares favourably to other studies, with the three highest resolution models showing a 9 % to 16 % increase (not monotonically) in transport relative to the coarse model (*Beckmann et al.* 1994, *Smith et al.* 2000, *Oschlies* 2002). However, the modeled transport remains smaller than the observed estimate of 88 Sv along 68° W made by *Johns et al.* (1995). The simulated maximum near-surface current speed along 68° W increases from 23.4 cm/s to 52.1 cm/s in going from 1.8°×3.6° to 0.2°×0.4°, but remains less than the observed value of 70 cm/s (*Johns et al.* 1995). The surface velocity field (not shown) confirms that the separation of the Gulf Stream into the Azores and North Atlantic Current (NAC) is significantly improved at higher resolution and corresponds with a greater poleward penetration of the NAC.

The dynamics of the North Atlantic subpolar gyre present an exceptional mod-

eling challenge due to the complex interaction between wind forcing, buoyancy contrasts and overflows from neighbouring seas. Detailed modeling studies have shown encouraging, but limited results in simulating observed currents and water mass characteristics in this region (*Willebrand et al.* 2001, *Treguier et al.* 2005). The overall structure and magnitude of the subpolar gyre transport remains fairly consistent with increasing resolution in this study (Fig. 3.2). However, the maximum transports of the subpolar gyre (Table 3.1) are low in comparison to regional models, one of which (the French ATL model) showed an increase in the maximum transport from 25 Sv to 40 Sv upon switching from coarse to high resolution (*Treguier et al.* 2005). This likely follows from the use of the same topography at coarse and high resolutions. An increase in the transport off the coast of Labrador in these models results from the penetration of the subpolar gyre further into the Labrador sea at higher resolution. The maximum near-surface speed of the Labrador current at 55° W (Table 3.1) increases from 3.5 cm/s to 17.4 cm/s between the coarsest and highest resolution models, but remains low in comparison to the observed values of roughly 30 cm/s (*Flatau et al.* 2003) .

3.3.2 Atlantic Meridional Overturning Circulation

AMOC transport in the model is depicted by the annual mean stream function of the zonally-integrated volume transport. Figure 3.3a shows that 21 Sv of NADW formation occurs in the 1.8°×3.6° model, although with a maximum poleward extent of 60° N it has a tendency to form too far south. This deficiency results from the models inability to transport surface waters effectively across the Iceland-Faroes ridge, which leads to the AMOC not penetrating far enough into the Greenland-Iceland-Norwegian (GIN) Seas (*Weaver et al.* 2001). Observational estimates of the present-day NADW volume transport range from 13-23 Sv (*Ganachaud and Wunsch* 2000, *Smethie and Fine* 2001, *Lumpkin and Speer* 2003, *Talley et al.* 2003). Approximately 1.5 Sv of Antarctic Bottom Water (AABW) is found extending to 25° N and fills the North

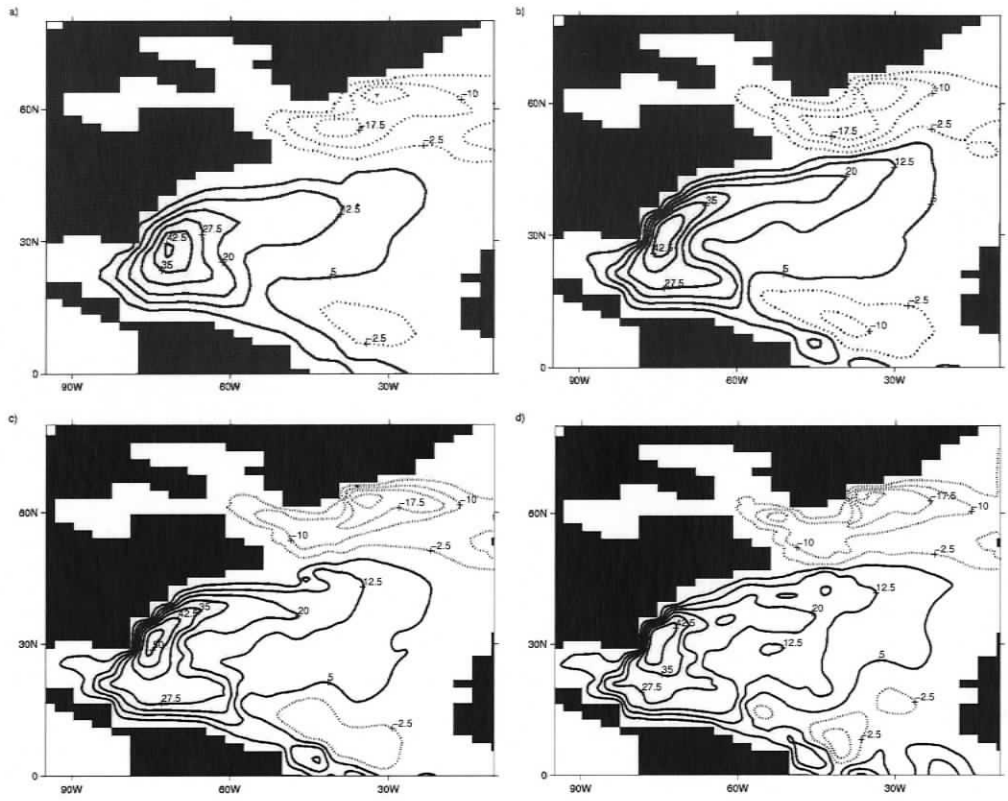

Figure 3.2: (a-d) Annual mean barotropic stream function (Sv) for the North Atlantic in the control runs at horizontal resolutions of $1.8° \times 3.6°$, $0.6° \times 1.2°$, $0.3° \times 0.6°$ and $0.2° \times 0.4°$, respectively. Dotted lines are negative.

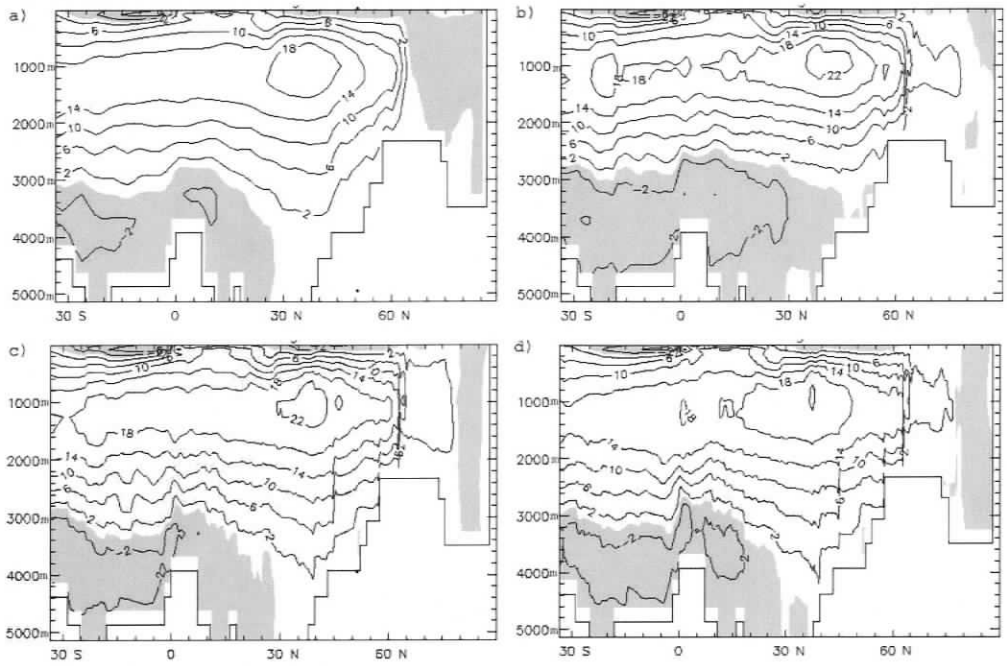

Figure 3.3: (a-d) Annual mean meridional overturning stream function (Sv) for the North Atlantic in the control runs at horizontal resolutions of $1.8°\times3.6°$, $0.6°\times1.2°$, $0.3°\times0.6°$ and $0.2°\times0.4°$, respectively. Shaded regions are negative.

Atlantic below 3000 m.

There is little difference in the overall structure and magnitude of AMOC transport among the three higher resolution models. In comparison to the $1.8°\times3.6°$ model, there is an increase of $1-2$ Sv in NADW formation and a significantly improved poleward penetration to 75° N. AABW transport increases slightly in these runs and extends slightly further north. The most significant change in AABW transport is found in the $0.6°\times1.2°$ model, with 2.5 Sv of transport at 25° N and 0.5 Sv extending to 40° N.

3.3.3 Meridional Heat Transport

Ganachaud and Wunsch (2003) used observational data to estimate the present-day, global ocean poleward heat transport to be 1.8 ± 0.25 PW (PW$\equiv 10^{15}$ watts) at 24° N, with ~ 70 % occurring in the Atlantic. Studies have shown the large-scale ocean heat transport to be dominated by the mean circulation (*Wunsch* 1999, *Talley* 2003).

However, locally the heat transport by small-scale and time-varying circulations can be of first order importance, influencing the large-scale heat transport directly via advection and indirectly by modifying the mean flow and surface heat flux budgets (*Stammer* 1997). Regional modeling studies have demonstrated a dependence of ocean heat transport on resolution, with coarse resolution models generating poleward transports that are significantly less than observed (*Fanning and Weaver* 1997, *Bryan and Smith* 1998).

The global ocean meridional heat transport increases with increasing resolution, while maintaining the same transport profile (Fig. 3.4). Each model exhibits poleward transport at all latitudes and a strong asymmetry across the equator. At 24° N there is almost a 30% increase in total oceanic heat heat transport (1.2 PW to 1.5 PW) by changing from 1.8°×3.6° to 0.2°×0.4° resolution. The increase in transport is likely associated with the better resolution of the western boundary currents in the baroclinic gyre circulations, which are significant components of the transport in the mid to high latitudes (*Fanning and Weaver* 1997, *Bryan and Smith* 1998). These results demonstrate that increases in horizontal resolution produce meridional heat transports that are closer to observed values. However, we also note that the 0.3°×0.6° model has slightly more heat transport (1.7 PW at 24° N) than the 0.2°×0.4° model.

3.3.4 NADW Formation

Open ocean deep convective mixing, triggered by extreme surface cooling events during the North Atlantic winter, is an important process in the formation of NADW (*Weaver and Hughes* 1992, *Dickson and Brown* 1994, *Marshall and Schott* 1999). The methods used to parameterize this process in models are widely debated (*Canuto et al.* 2004, *Treguier et al.* 2005). The UVic ESCM employs an explicit full convection scheme, which includes diagnostics to save the ventilation depth and potential energy released by convection at each grid point (*Pacanowski* 1995).

Figure 3.5 shows the depth of convective activity in the North Atlantic averaged

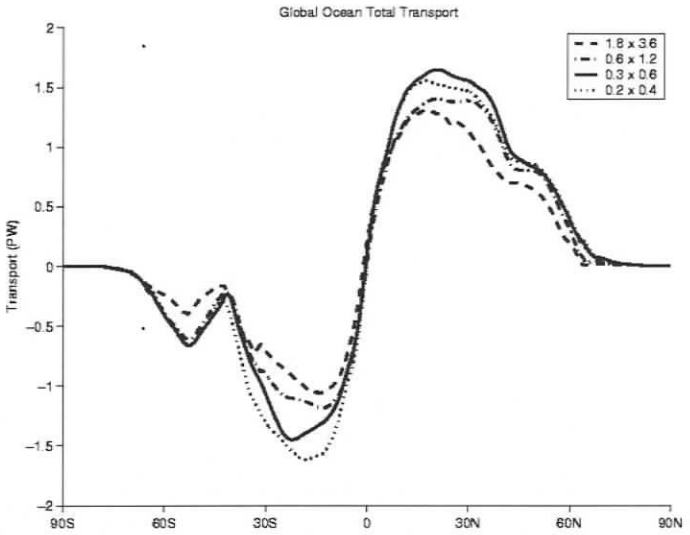

Figure 3.4: The total meridional heat transport for the global ocean at each model resolution.

over the winter months (January, February and March) in the last year of the control runs. None of the models exhibit a significant amount of interannual variability in the magnitude or location of convection. In all four models, deep (> 300 m) convective activity occurs predominately in the GIN Seas, albeit too far south. While the poleward penetration of the NAC is improved at higher resolution, it apparently still does not transport surface waters across the Iceland-Faroes ridge effectively enough to provide suitable conditions for deep convection. The most striking difference between models is the occurrence of convective activity in the Labrador Sea, and to a lesser extent the Irminger Sea, in all but the coarsest resolution model. To quantify this difference the potential energy released by deep winter convection is summed over the entire subpolar gyre region and exclusively over the Labrador Sea (Fig 3.5a defines these regions). The results, shown in Table 3.1, demonstrate a significant contribution from the Labrador Sea to the total convective energy in all but the coarsest model. The depth of Labrador Sea convection compares well with the observations of *Lavender et al.* (2002). There is also a 15% decrease in the total Atlantic convective energy in the two eddy-permitting models.

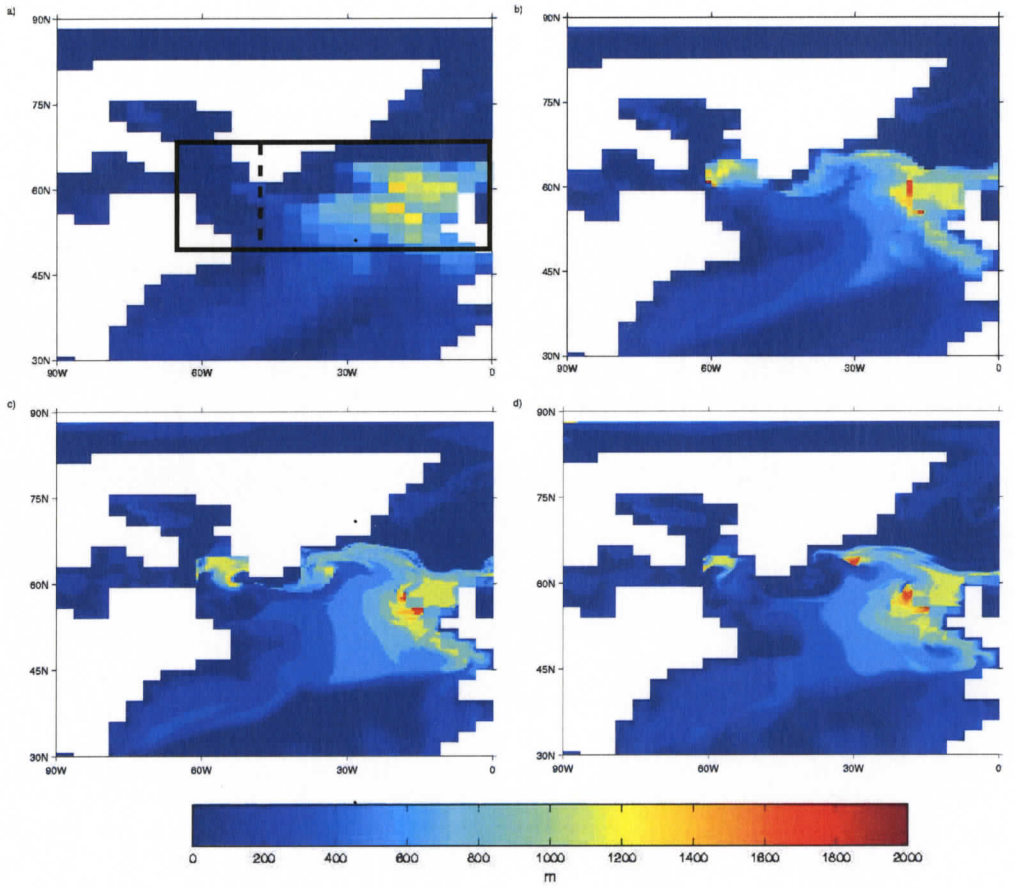

Figure 3.5: (a-d) Ventilation depth of convective activity in the North Atlantic averaged over the months of January, February and March in the last year of the control runs at horizontal resolutions of $1.8°\times3.6°$, $0.6°\times1.2°$, $0.3°\times0.6°$ and $0.2°\times0.4°$, respectively. The vertical dashed line extending southward from the tip of Greenland in (a) distinguishes the Labrador Sea region from the total area (indicated by the large black box) where the potential energies for Table 3.1 were calculated.

In order to evaluate how differences in the location of convective activity effects the formation of NADW three inert tracers are applied to the ocean surface in the 1.8°×3.6°, 0.6°×1.2° and 0.3°×0.6° control runs. Computational constraints prevented us from applying tracers in the 0.2°×0.4° model. Tracer one was applied to the region of convective activity in the GIN Seas, tracer two was applied to the Labrador Sea and tracer three was applied everywhere else in the global ocean (hereafter referred to as the LAB tracer, GIN tracer and GLOBAL tracer, respectively). A constant flux (0.1 Sv) of each tracer was applied to the ocean surface in each control run and integrated in parallel with the freshwater forcing runs (in which tracers were also applied) for an additional 50 years. The percentage and location of NADW that originated at the surface of the Labrador and GIN Seas (ignoring advection of the tracers at the surface) is estimated by zonally integrating the three tracers across the Atlantic basin and then calculating the percentage of each relative to the total amount of tracers in a grid cell. Figure 3.6 shows the distribution of tracers in the 1.8°×3.6° and the 0.3°×0.6° models after 50 years. The 0.3°×0.6° model fairly represents the tracer distributions in the 0.6°×1.2° model that also exhibits extensive convection in the Labrador Sea. It should be noted that very small amounts of tracers are found below 4000 m, resulting in tracer percentages that are not indicative of significant amounts of NADW.

The models clearly simulate the sinking and spreading of NADW below the permanent thermocline to a depth of 3500 m at 30° S, where after 50 years the tracers tend to accumulate and override AABW. Figure 3.6 further reveals significant differences between models in the surface source regions of NADW. In the 1.8°×3.6° model, $\sim$ 5 % of NADW originated in the Labrador Sea (Fig. 3.6a), while GIN tracers comprise $\sim$ 55 % (Fig. 3.6b). In the 0.3°×0.6° model, $\sim$ 15 % of NADW originated in the Labrador Sea (Fig. 3.6c), while $\sim$ 35 % of the tracers originated at the surface of the GIN Seas (Fig. 3.6d). The GLOBAL tracer makes up the residual percentages,

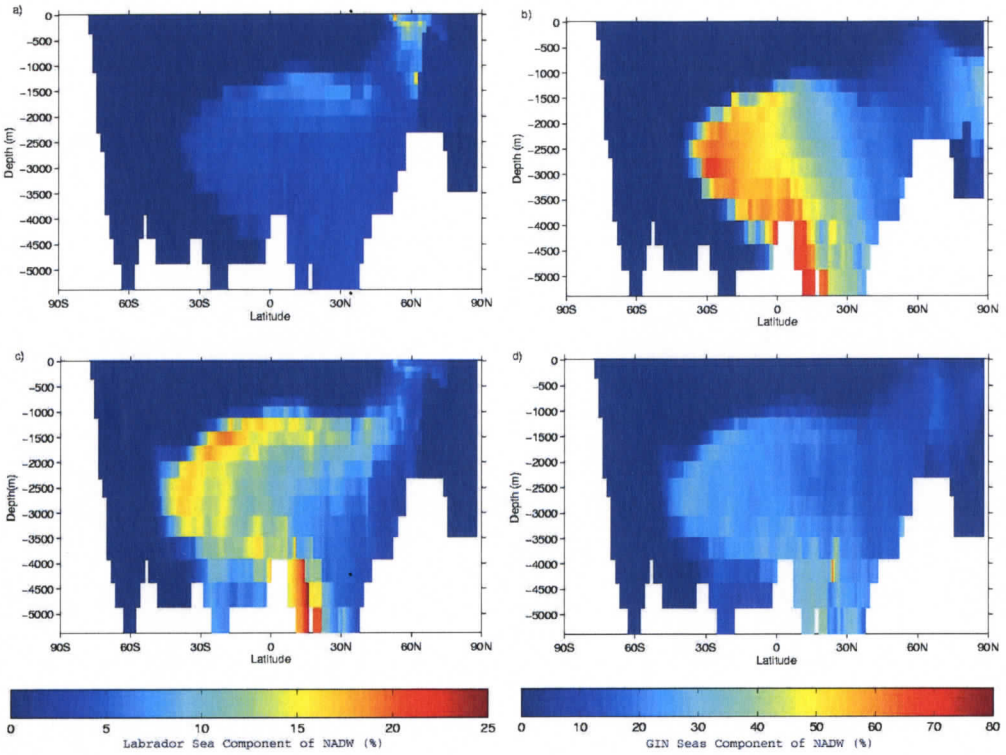

Figure 3.6: (a) and (c) show the percentage of NADW identified by tracers to have originated in the Labrador Sea for the 1.8°×3.6° and 0.3°×0.6° models, respectively. Similarly, (b) and (d) show the percentage of NADW that originated in the GIN Seas. Different color bar scales are used for the GIN and LAB tracers percentages.

which amounts to roughly ~ 40 % and ~ 50 % for the 1.8°×3.6° and 0.3°×0.6° models, respectively. Figure 3.6 shows that while similar amounts of NADW are formed, a greater percentage of it originated at the surface of the Labrador Sea in the higher resolution model.

3.3.5 Sea Ice Distribution

At its standard resolution (1.8°×3.6°) the UVic ESCM produces sea ice climatology that, relative to other GCMs, favourably compares to observations (*Weaver et al.* 2001). However, the fact that NADW forms too far south leads to a sea ice cover that extends too far south in the North Atlantic, especially in the GIN Seas (Fig. 3.7a). As horizontal resolution is increased, there is a significant reduction in North Atlantic sea

ice extent; particularly in the region of the Norwegian Current, and to a lesser extent in the Labrador Sea and Hudson Bay (Fig. 3.7b-d). The annual average northern hemisphere sea ice area in the 1.8°×3.6° model is 9.0×10^{12} m^2. The simulated sea ice area is reduced by 6.7 %, 10.0. % and 11.9% as resolution is increased to 0.6°×1.2°, 0.3°×0.6° and 0.2°×0.4°, respectively. Observations from the late 1980s estimated the annual average northern hemisphere sea ice area to be about 11.5×10^{12} m^2 (*Peixoto and Oort* 1993). The annual average northern hemisphere sea ice volume in the 1.8°×3.6° model is 9.3×10^{12} m^3. It is reduced by 6.5 %, 8.6 % and 9.2% as resolution is increased to 0.6°×1.2°, 0.3°×0.6° and 0.2°×0.4°, respectively. Highly uncertain observations from the early 1980s estimated the annual average northern hemisphere sea ice volume to be about 3.0×10^{12} m^3 (*Hartmann* 1994). The monotonic pattern of North Atlantic sea ice reduction in response to increased horizontal resolution is consistent with the findings of increased meridional heat transport and greater poleward penetration of AMOC surface waters at higher resolutions.

3.4 Response to 8.2 kyr Event Freshwater Forcing

3.4.1 AMOC Response

The principal means of detecting changes in NADW formation is to examine changes in the maximum value of AMOC transport between the latitudinal bounds of 26° N and 70° N, and depths of 170 m and 4000 m (AMOC strength hereafter). The 1.8°×3.6° model produces a pre-industrial equilibrium AMOC strength of 21 Sv with little internal variability (Fig. 3.8). At 0.6°×1.2° and 0.3°×0.6° the AMOC equilibrates at $\sim$ 23 Sv, while at 0.2°×0.4° the AMOC strength tends to decline slightly from $\sim$ 23 Sv to $\sim$ 21.5 Sv prior to forcing (Fig. 3.8). The internal variability in NADW formation is significantly increased in the three highest resolution models.

The overall response of the AMOC to the LAB forcing scenario is consistent among the models (Fig. 3.8a). All exhibit near immediate reductions in the rate of

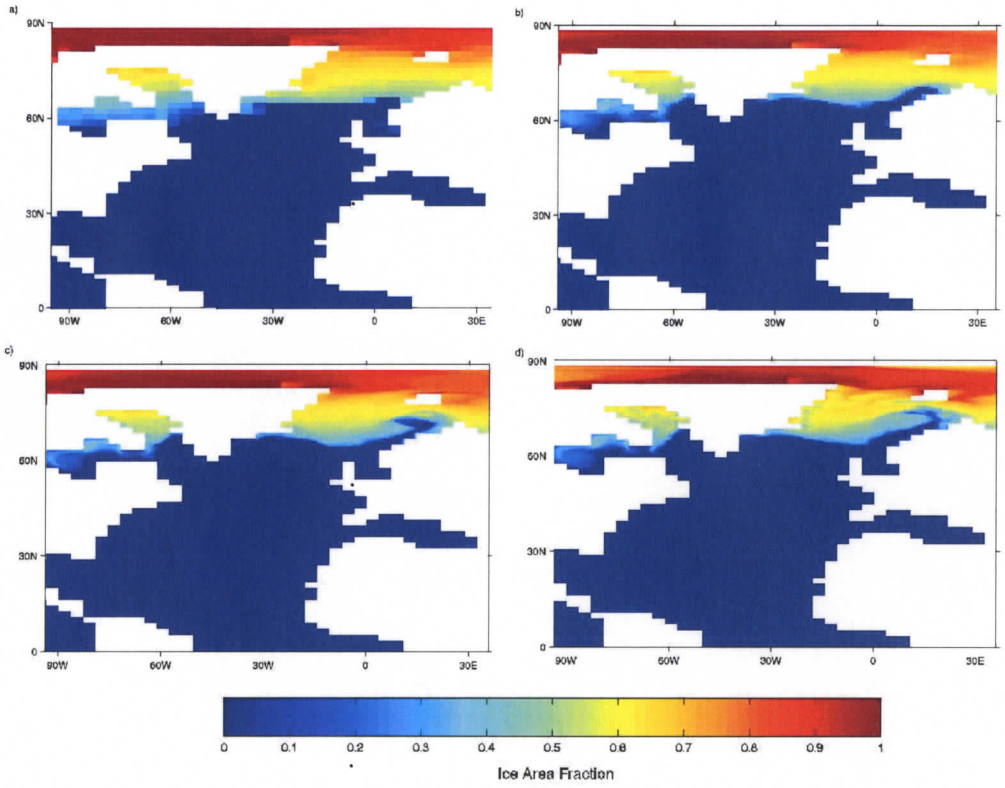

Figure 3.7: (a-d) Annually averaged fraction of each ocean grid cell covered by ice at horizontal resolutions of $1.8° \times 3.6°$, $0.6° \times 1.2°$, $0.3° \times 0.6°$ and $0.2° \times 0.4°$, respectively.

NADW formation and subsequently recover. The total duration (ranges from 40-60 years) and maximum amplitude (ranges from 4-7 Sv) of the AMOC response does not have a consistent dependence on model resolution. However, there are subtle differences in the pathway of the response. The initial decline in the $1.8° \times 3.6°$ is followed by a brief period of reintensification (starting 5 years after forcing) before smoothly recovering, in accord with the coarse resolution model results presented by (*Manabe and Stouffer* 1995, *Renssen et al.* 2002, *Bauer et al.* 2004). Over the first 10 years the $0.6° \times 1.2°$ model follows a similar path as the $1.8° \times 3.6°$ model, but has a second reintensification phase (20 years after forcing) that precedes another relatively small decline in AMOC strength before recovery. Neither the $0.3° \times 0.6°$ or $0.2° \times 0.4°$ models show a reintensification phase within the first 10 years. Instead they exhibit a reintensification similar to the the second phase of the $0.6° \times 1.2°$ model.

There are substantial differences in the pathway of the AMOC response to the BC forcing scenario (Fig. 3.8b). First, all four models exhibit a strong reintensification within the first 5 years of the response. The three highest resolution models also show a substantial second reintensification that is followed by a significant third phase of reduced NADW formation before recovery. While the maximum amplitude of decline in AMOC strength and total duration of the response are similar to that found for the LAB forcing, there are higher amplitude variations in the response of all four models.

3.4.2 Surface Air Temperature Response

The amplitude of maximum cooling in transient response of the annual average northern hemisphere surface air temperature (SAT) is fairly insensitive to differing model resolutions and forcing regions (Fig. 3.9). A rapid cooling of roughly 0.4° C within the first 5 years is found in all models for both the BC and LAB scenarios. The amplitude of this cooling is of the same order of magnitude as observed interannual SAT variability (see Figure 12.7 of *McAvaney et al.* (2001)) and would be difficult

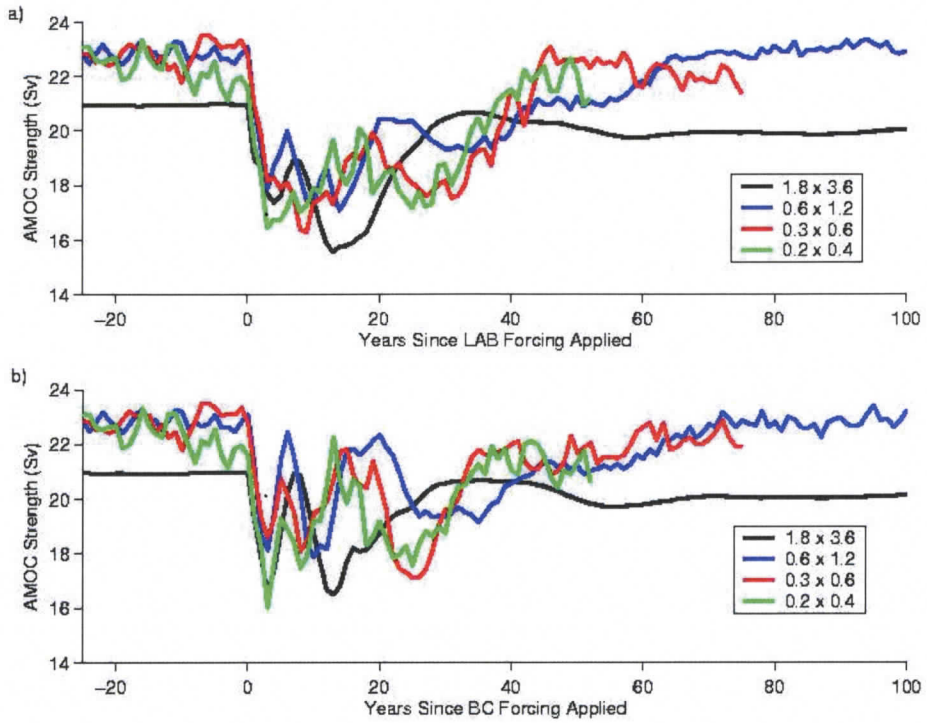

Figure 3.8: The AMOC strength of each model over the 25 year period prior to forcing, and the response to the LAB (a) and the BC (b) freshwater forcing scenarios.

to detect from paleo-reconstructions. The cold period is sustained for at most a few years as it enhances the meridional temperature gradient, which induces a poleward advection of heat in the North Atlantic. In the three higher resolution models there is a second cooling phase due to the lagged restoration of deep convection in the Labrador Sea (*Manabe and Stouffer* 1995, *Renssen et al.* 2002). After 20 years the northern hemisphere SAT recovers, exceeding the pre-forcing values by $\sim 0.1°$ C in all but the highest resolution model. The total duration of the SAT response (50 years) is consistent among the models, but much shorter than the 200 year anomaly inferred from paleodata. Previous studies highlighted the importance of long term changes in the routing of glacial runoff, along with the abrupt drainage of Lake Agassiz, as an important mechanism for extending the duration of the 8.2 kyr event (*Bauer et al.* 2004, *Meissner and Clark* 2006).

The spatial pattern of the SAT response to the LAB forcing is also relatively insen-

sitive to increasing model resolution. Global SAT anomalies 5 years after the initial forcing for the 0.3°×0.6° model are representative of the other models (Fig. 3.10a). The SAT decreases by 0.4-2.4°C over the North Atlantic and Europe, which is within the range of estimates from paleorecords (*Bond et al.* 1997, *von Grafenstein et al.* 1998). A warming signal in the range of 0.2-0.6° C is found poleward of 30° S that is consistent with the inter-hemispheric see-saw nature of heat transport identified in previous modeling studies (*Stocker* 1998).

All models produce less cooling in the subpolar west Atlantic and more cooling in the subpolar east Atlantic in response to the BC forcing (Fig. 3.10b). This effect is enhanced with increasing resolution: the maximum positive difference in the west and negative difference in the east increases from 0.45° C to 0.75° C and -0.18° C to -0.50° C, respectively, with resolution. A recent study by *Saenko et al.* (2007a) explored the mechanism that led to an extensive area of the subpolar west Atlantic actually warming when freshwater is discharged along the Labrador coast, despite a substantial weakening of the AMOC. They used a coarse resolution model with ocean and sea ice components similar to that employed here, but included a more complex atmospheric component that allowed surface wind anomalies to feedback on the ocean. Their experiment also started from a cooler intial state with more extensive Labrador Sea ice coverage, the melting of which is required to amplify the warming response. *Saenko et al.* (2007a) show that the mechanism driving the warming is a retreat of sea ice in the subpolar Atlantic, maintained by changes in the local wind stress curl translating into changes in the oceanic convection.

3.4.3 NADW Tracer Ànomalies

The application of tracers in the 1.8 °×3.6°, 0.6°×1.2° and 0.3°×0.6° control runs alongside the freshwater forcing runs (refer to Section 3.3d) allows us to separately evaluate the effect of the forcing on NADW formed in both the Labrador and GIN Seas. Tracer anomalies are.calculated every 5 years as the percent difference between

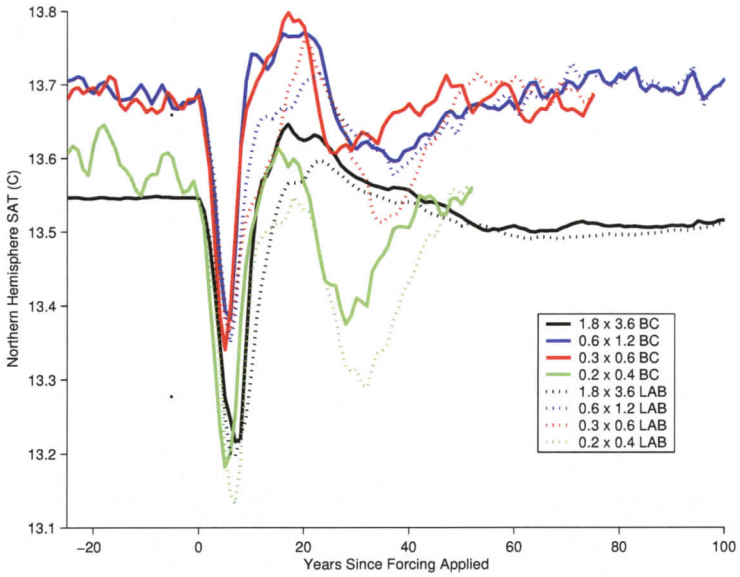

Figure 3.9: Northern hemisphere surface air temperature response to freshwater forcing.

the forcing and control runs in the amount of tracers found below 1000 m in the Atlantic. Anomalies after 15 years are evaluated to provide enough time for a significant amount of the tracers to be advected to depth.

The maximum reduction of GIN tracers ranges from 34-44 % (Fig. 3.11a). The reduction is smaller in response to BC forcing than to LAB forcing in all three models, with the maximum difference between forcing scenarios increasing from 3 % at 1.8 °×3.6° to 11 % at 0.3 °×0.6°. In response to the BC forcing, the reduction of GIN tracers is monotonically reduced as horizontal resolution is increased. There is not a consistent dependence on model resolution in the GIN tracer response to LAB forcing.

The reduction of LAB tracers are significantly larger than the reduction of GIN tracers in the 0.6°×1.2° and 0.3°×0.6° models (Fig. 3.11b). With a maximum decrease of 75 % in response to LAB forcing and 55% in response to BC forcing for both models, the LAB tracer response is substantially dependent on the forcing scenario in the two higher resolution models. There is little difference between forcing scenarios

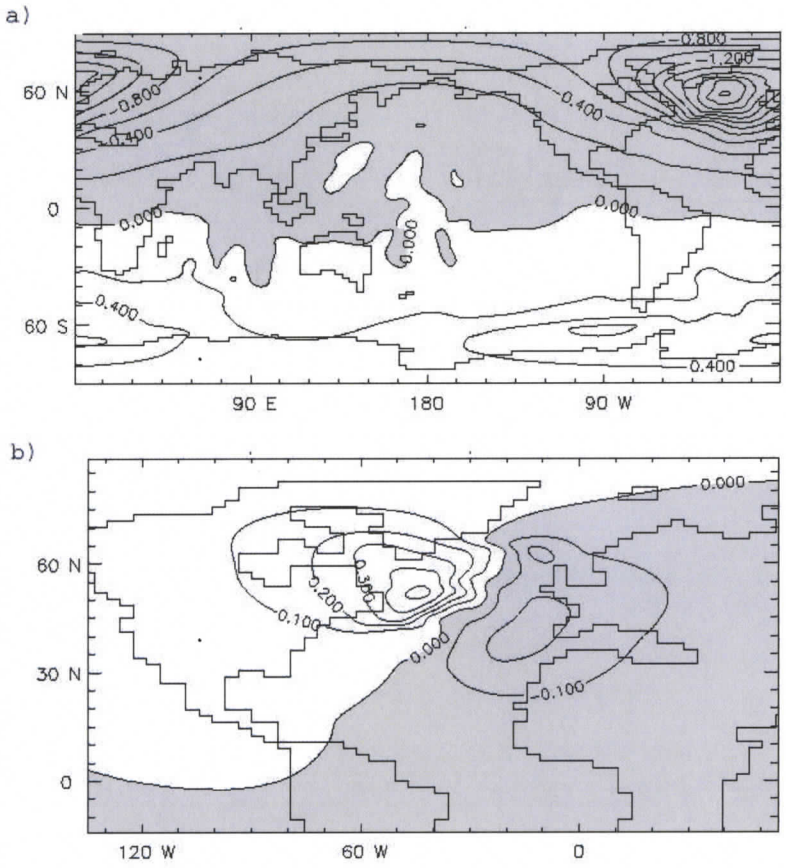

Figure 3.10: (a) The global SAT anomalies for the LAB forcing scenario and (b) the BC minus LAB forcing SAT difference in the North Atlantic 5 years after initial forcing at $0.3° \times 0.6°$ resolution. Shaded regions are negative.

in LAB tracer anomalies for the 1.8°×3.6° model. They increase from −20% to 25% after 25 years as the result of Labrador Sea convection actually turning on ∼ 10 years after the initial forcing. It is possible that convective activity in the North Atlantic has multiple stable states, and the forcing may have perturbed the coarse resolution model from a state where Labrador Sea convection is not favoured to one where it is.

It is interesting that the NADW tracer anomalies present a different and perhaps clearer perspective on the influence of horizontal resolution and forcing region than the AMOC strength. Overall the tracers show a weaker response to BC forcing than to LAB forcing, and this effect is enhanced with increasing resolution. Deep water formation in the Labrador Sea is also more affected than in the GIN Seas. It seems likely that the relative insensitivity of the AMOC response to increasing resolution is partially the result of increased deep convection in close proximity to the freshwater forcing regions in the higher resolution models.

3.5 Conclusions

This section investigated the sensitivity of a series of global climate models with increasing horizontal resolution to freshwater forcings similar to the 8.2 kyr event. First, the pre-forcing state of models at 1.8°×3.6°, 0.6°×1.2°, 0.3°×0.6°, and 0.2°×0.4° were evaluated. The representation of the barotropic volume transports in the North Atlantic are improved at higher resolution, and the speed of the western boundary currents off the coast of Florida and Labrador are increased by factors of two and five, respectively, from coarsest to highest resolution. Improvements in the meridional heat transport and the poleward penetration of the NAC result in a monotonic reduction in North Atlantic sea ice. While the AMOC remains stable in all models (NADW formation rates in the range of 21-23 Sv), the energy released by Labrador Sea deep convection is increased by roughly an order of magnitude at higher resolution.

The total duration (ranges from 40-60 years) and maximum amplitude (ranges

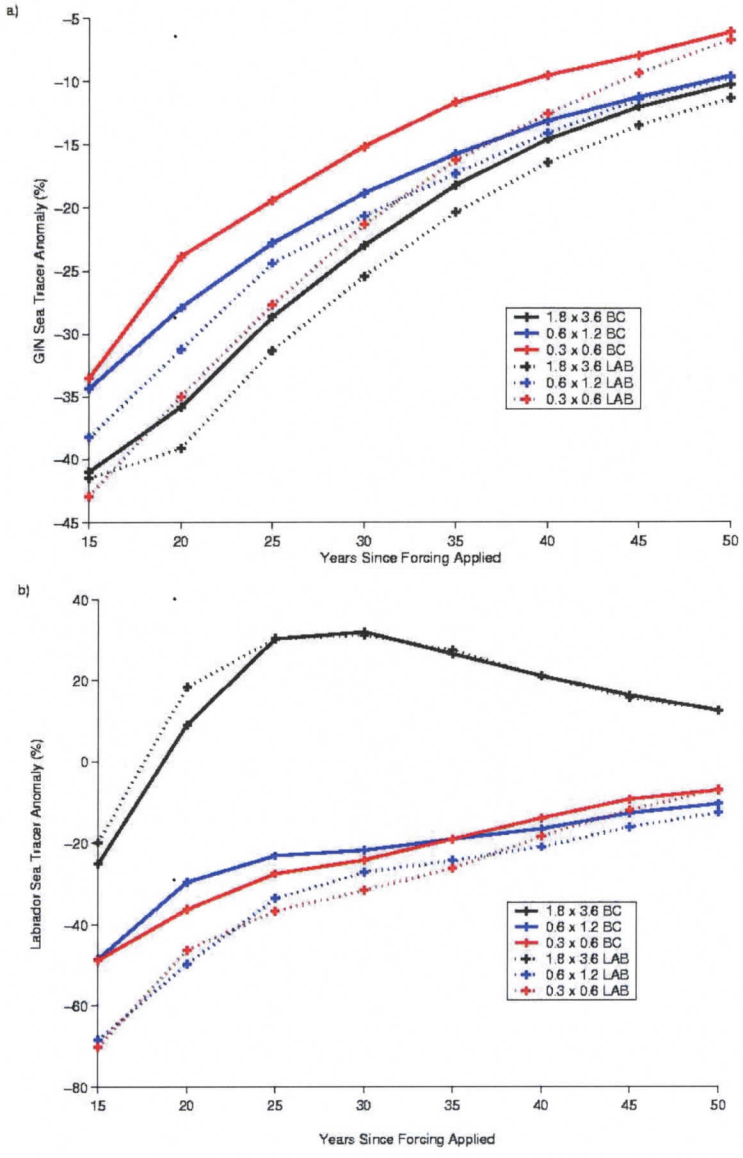

Figure 3.11: Percent difference in amount of tracers found below 1000m in the Atlantic Ocean relative to control runs (Frames a-b refer to tracers applied over the surface of GIN and Labrador Seas, respectively). Tracer anomalies are calculated every 5 years as the percent difference between the forcing and control runs in the amount of tracers found below 1000 m in the Atlantic. Anomalies after 15 years are evaluated to provide enough time for a significant amount of the tracers to be advected to depth.

from 4-7 Sv) of the AMOC response to freshwater forcing showed little sensitivity to increasing resolution and differing forcing regions. An evaluation of the forcing impact on different regions of NADW formation with tracers highlighted the possibility that increases in Labrador Sea deep convection at higher resolution mitigates the effects of stronger boundary currents and enhanced mixing. There were differences in the pathway of the AMOC response, with boundary current forcing producing significantly higher amplitude variability in NADW formation than Labrador Sea forcing. A monotonic effect with increasing resolution of less cooling in the subpolar west Atlantic and more cooling in the subpolar east Atlantic was also found in response to the boundary forcing. Since the UVic ESCM employs a simple, vertically integrated atmospheric component, a significant caveat to these results is the possible importance of a more detailed and dynamic representation of the surface winds and storm tracks.

These results are reassuring in showing that the response of a coarse resolution EMIC to 8.2 kyr event freshwater forcing is comparable to that at ocean eddy-permitting resolutions. While subtle differences exist, the coarse resolution AMOC response remains robust at finer horizontal resolutions.

Chapter 4

The Southern Ocean Overturning: Response to Anthropogenic Forcing

4.1 Introduction

The upper ocean MOC can be thought of as consisting of two branches (*Gnanadesikan* 1999). One is associated with deep water formation in the northern North Atlantic where light waters are converted to dense waters. In the other branch, found in the Southern Ocean and in the low-latitude oceans, the reverse process takes place with dense water being converted back to light water. The two branches can influence each other in that, for example, a change in the dense-to-light water conversion in the Southern Ocean could translate into a change in the light-to-dense water conversion in the north, and vice versa. In models, the degree of this north-south connection may depend on the representation of the individual components of the MOC. In particular, coarse resolution models that capture only the large-scale features of the circulation are obliged to parametrize the effects of unresolved mesoscale motions, i.e. the motions which account for most of the kinetic energy in the ocean (e.g., *Ducet et al.* (2000), *Wunsch* (2007)). In the Southern Ocean, where mesoscale eddies play a fundamental role in closing the MOC, there is a particular need to rely on such parametrizations.

One of the most, if not the most widely employed schemes to parametrize the effect of mesoscale eddies on tracer transport and, hence, on large-scale circulation is that of GM90. It has been shown in many studies that the GM90 scheme is capable of greatly improving the interior tracer distribution and can strongly influence the simulated MOC (e.g., *Danabasoglu et al.* (1994), *Wiebe and Weaver* (1999)). There are, however, unresolved questions. For example, *Hallberg and Gnanadesikan* (2006) question the ability of coarse-resolution models employing the GM90 scheme to accurately capture the impact of changes in the Southern Ocean winds on the MOC. Furthermore, *Hirst and McDougall* (1998) argue that it is not clear if the GM90 eddy-induced transport can actually be interpreted as a "bolus" transport arising from unresolved temporal correlations between varying isopycnal surfaces and velocities. They show in a coarse resolution model that while the GM90 eddy-induced transport could combine with "resolved" transport to produce a total (or residual) circulation that would tend to follow isopycnals in the interior, such a near-adiabatic nature of the circulation may not always hold for large-scale and eddy-induced flows separately. Thus, the eddy-induced circulation due to GM90 may lead to strong cross-isopycnal flows in coarse-resolution models (e.g., *Hirst and McDougall* (1998), *Speer et al.* (2000a), *Saenko et al.* (2005), *Gent et al.* (1995). Therefore, it remains unclear if the circulation induced by the parametrized eddies can be employed for tracking the pathways of the transport induced by "permitted" eddies. In addition, as resolution increases the simulated western boundary currents – an important component of the MOC – become less viscous, so that an input of vorticity due to the wind stress curl is expected to be mostly balanced by bottom pressure torques rather than by lateral viscous stresses (*Hughes* 2000). Furthermore, the influence of the subgrid scale processes arising from convection and small-scale turbulent mixing may also depend on resolution. All these factors have the potential to produce substantial differences between simulations of the ocean circulation by coarse resolution and eddy-permitting

models, including such an integral quantity as the MOC.

The aim here is to employ four versions of the same model, ranging in horizontal resolution from coarse to (marginally) eddy-permitting, in an attempt to understand how the simulated MOC depends on resolution. The focus of this study is on the Southern Ocean, and an attempt is made to connect the MOC to the local buoyancy input at the surface, following the approach first proposed by *Walin* (1982). Section 4.2 describes the experimental design. The effect of increasing resolution on a near pre-industrial (year 1900) control state of the MOC and transformation rates are analyzed in section 4.3. Section 4.4 evaluates their response to observed and projected poleward intensifying southern hemisphere winds concomitant with increasing atmospheric CO_2 through the 21st century – a topic which is of major interest to the climate modelling community (*Fyfe et al.* 2007, *Treguier et al.* 2007, *Zickfeld et al.* 2007). A discussion and conclusions are presented in section 4.5.

4.2 Experimental Design

UVic ESCMs with horizontal resolutions of $0.6°\times1.2°$, $0.3°\times0.6°$ and $0.2°\times0.4°$ are initiated from the interpolated 3000 year equilibrium state of a $1.8°\times$ $3.6°$ model. They are equilibrated under pre-industrial (year 1900) orbital, atmospheric and land surface conditions. Table 4.1 lists the values of the primary parameters modified in each model as well as their integration periods. Following the resolution criterion of *Bryan et al.* (1975), the horizontal mixing coefficient for momentum is reduced by roughly the factor increase in resolution (isopycnal tracer mixing coefficients were similarly reduced). Using this criterion, in the base-line model with the highest resolution ($0.2°\times0.4°$) the Laplacian viscosity coefficient is set to a relatively large value of $1.5\times10^4 m^2 s^{-1}$ (Table 4.1). To make the dissipation more scale selective, one possibility is to employ the biharmonic form for lateral viscosity. However, this would require introducing different parametrizations for the different model resolutions –

something chosen to be avoided in this intercomparison study. On the other hand, it is worthwhile to make a link with existing eddy-permitting models of the same or comparable resolution, such as the Fine Resolution Antarctic Model (FRAM). The FRAM model is a primitive equation numerical model of the Southern Ocean (between 24°S and 79°S) which has the horizontal resolution of $0.25° \times 0.5°$. It was started with a Laplacian viscosity of $0.2 \times 10^3 m^2 s^{-1}$ and subsequently switched to biharmonic viscosity (*The FRAM Group (D. Webb et al.)* 1991). Therefore, in addition to the base-line experiments listed in Table 4.1, two experiments with the $0.2° \times 0.4°$ model are discussed, wherein the Laplacian viscosity coefficient was decreased to $10^3 m^2 s^{-1}$ and to $0.2 \times 10^3 m^2 s^{-1}$. These were run for only 5 years, starting from the final control state (year 50) of the $0.2° \times 0.4°$ base-line model run. The decrease of the viscosity coefficient results in an increase of eddy kinetic energy (EKE). In particular, averaged around 55°S, the near-surface EKE increases from 27 $cm^2 s^{-2}$ in the base-line $0.2° \times 0.4°$ model to 93 $cm^2 s^{-2}$ when the horizontal viscosity is decreased to that of FRAM model (zonally-averaged EKE at 55°S is estimated from satellite altimetry to be 314 $cm^2 s^{-2}$; C. Wunsch, personal communication, 2008). The filaments and plumes that characterize the Agulhas retroflection region of the base-line $0.2° \times 0.4°$ model are found to generate more realsitic warm core eddies in the reduced viscosity runs. It should, however, be noted that at this resolution such a reduction of the viscosity coefficient is expected to violate the *Bryan et al.* (1975) stability criterion (see also Appendix A), so that these additional runs are given only a brief discussion. On the other hand, the applicability of the *Bryan et al.* (1975) linear criterion to coupled model solutions based on primitive equations is not quite clear (e.g., *Jochum et al.* (2008)).

While the horizontal resolution of each model component (ocean, land, atmosphere and sea ice) is increased, only the ocean employs resolution dependent surface data. Resolution dependent bathymetry data was created for the three higher resolu-

Table 4.1: Horizontal resolution parameters and integration periods of Southern Ocean forcing simulations

Horizontal Resolution	1.8°×3.6°	0.6°×1.2°	0.3°×0.6°	0.2°×0.4°
$\boldsymbol{A_M}$ **(**$\times 10^4 \mathbf{m^2/s}$**)**	20	7	3	1.5
$\boldsymbol{A_{ISO}}$ **and** $\boldsymbol{A_{ITH}}$**(**$\times 10^2 \mathbf{m^2/s}$**)**	4	1.5	1	0.75
Control Integ. Length (years)	3000	450	100	50
Forcing Integ. Period (year)	1900-2100	1900-2100	1900-2100	1900-2080

A_M, A_{ISO} and A_{ITH} are the horizontal viscosity, isopycnal diffussion and isopycnal thickness diffusion coefficients, respectively. The three highest resolution models were initiated from the 3000 year equilibrium state of the 1.8°× 3.6° model.

tion models by averaging the National Geophysical Data Center 5 arc minute gridded relief dataset (*NGDC* 2007). The number of land masses and the shape of coastlines were held fixed as resolution increased by placing a minimum 125 m (ocean level 2) depth constraint on new bathymetry features. All models have 19 vertical ocean levels and the same vertical ocean mixing coefficients. The vertical resolution is lower than in the FRAM, but is comparable to that employed in some global eddy-permitting ocean models (e.g. *Semtner and Chervin* (1988)). A coarse vertical resolution was the computational sacrifice required to evaluate the overturning circulation in century rather than decade long eddy-permitting simulations.

The integration times of the two highest resolution models are still not sufficient to remove all long timescale ocean transients induced upon switching resolution. Timestep interval data from these models show weak trends in global ocean potential temperature and salinity of roughly +0.03 K/century and +0.0040 psu/century, respectively, after switching resolution. The range of global mean ocean potential temperature and salinity among the models is 3.35 K to 3.60 K and 34.79 psu to 34.80 psu, respectively.

Models are forced from their control state with annually varying CO_2 concentrations and monthly surface wind anomalies. Computational constraints limit the

forcing period of the $0.2° \times 0.4°$ simulation to 180 years (1900 to 2080); the three coarser resolution models are integrated to 2100. The CO_2 concentration follows observations (295 ppm to 365 ppm) over the first 100 years, and then increases to 830 ppm by 2100 following the IPCC SRES-A2 scenario. Surface wind anomalies were assembled from a series of simulations performed by ten different global climate models (forced by the same historical and SRES-A2 emissions trajectory) in support of the IPCC Fourth Assessment Report. Model-mean wind anomalies relative to 1900 were computed, temporally smoothed, corrected for a small equatorward bias (*Fyfe et al.* 2007), and then added to the NCEP50 climatology in the southern hemisphere only. The maximum zonal wind stress in the southern hemisphere increases by about 25% and shifts poleward by roughly 3.5° by the end of the 21st century.

4.3 Evaluation of Control Climate

4.3.1 Overturning Circulation

Since our focus is on the circulation in the meridional plane, it is relevant to consider a theory which assumes some kind of zonal averaging. In general, the issue of zonal averaging is important and not trivial. For example, one could apply zonal averaging along latitude circles; alternatively, it could be done along mean streamlines of the Antarctic Circumpolar Current (ACC) (e.g., *Treguier et al.* (2007)) or along mean buoyancy surfaces (e.g., *Döös and Webb* (1994)), or both. Each of these formulations has advantages and disadvantages. For example, the mean position of ACC is expected to vary with depth, whereas the isopycnal framework can be problematic near the surface where isopycnals outcrop in the presence of eddies. It is for the latter reason that the preference is often given to z coordinates.

In the oceanic interior where diabatic processes are weak, the circulation is expected to follow isopycnal surfaces. The position of these surfaces can significantly deviate from the surfaces of equal depth or pressure. Therefore, using potential den-

sity as the vertical coordinate, rather than more traditionally used depth or pressure, can result in some major differences in the way the MOC is displayed. This was first illustrated by *Döös and Webb* (1994) and also by *McIntosh and McDougall* (1996) using a fine resolution model of the Southern Ocean. It was shown, in particular, that the so-called "Deacon cell", which normally appears when MOC is plotted as a function of depth, results from branches of equatorward and poleward flow occurring at the same densities but slightly different depths. The cell is characterized by an apparent sinking of surface waters to depths of 1000-3000 m between 40°-50°S, creating an impression of mass flux across density surfaces. *Döös and Webb* (1994) demonstrate that Deacon cell is much reduced if instead of depth one uses potential density as the vertical coordinate.

Herein the meridional circulation is evaluated in density coordinates by first binning ocean model data onto 51 potential density levels with the difference between successive levels linearly decreasing from 0.3 kg m^{-3} to 0.085 kg m^{-3} as density increases. The choice of a reference density coordinate is known to affect the appearance of the overturning circulation (*Hirst and McDougall* 1998, *Döös and Webb* 1994). The resolution dependence of the overturning circulation is evaluated with a potential density coordinate referenced to 3000 m depth (σ_3) in order to clearly show intermediate depth waters.

Following *Döös and Webb* (1994) and *Döös et al.* (2008, 2009), the streamfunction as a function of density is calculated as follows:

$$\Psi_{res}(y,\sigma_3) = \frac{1}{t_1 - t_0}\int_{t_0}^{t_1}\oint\int_{-H(x,y)}^{z(x,y,\sigma_3,t)} v(x,y,z,t)dzdxdt, \tag{4.1}$$

where $v(x,y,z,t)$ is the meridional velocity binned into the (varying in time and space) σ_3 surfaces, $z(x,y,\sigma_3,t)$. This calculation is compatible with mass conservation in the model in that the overturning steamfunction integrated from the bottom

goes to relatively small values at the surface (it is expected that because of the implicit free-surface formulation employed in the model, the steamfunction corresponding to instantaneous flows may not always be closed; since the emphasis here is on the deeper ocean, the integration in Eq. 4.1 is taken from the bottom).

Calculated this way, the "residual" streamfunction, Ψ_{res}, contains both the contribution from the time-mean circulation and that due to eddies (at eddy-permitting resolution), with the latter resulting from correlation between varying in time velocity and density. To represent the evolution of v and σ_3, snapshots are used that are taken 5 days apart over a time integration interval of t_1 - t_0 equal to one year. As pointed out by *McIntosh and McDougall* (1996), and illustrated in *Döös et al.* (2009), in a model where there is no strong interannual forcing, such as employed here, using several years of snapshots instead of one year should not result in significant changes in this type of calculation. An integration interval of three years was tested for the $0.2°\times0.4°$ simulation and did not find a significant difference.

Figure 4.1 shows the residual MOC in the Southern Ocean calculated for the four different model resolutions. In each case, the meridional velocity represents the so-called effective transport, which is given by the sum of the resolved velocity and that due to the GM90 parametrization. However, the latter has a negligible influence on Ψ_{res} at $0.2°\times0.4°$, whereas its influence increases with the decrease in the model resolution. Of particular interest is the clockwise circulation associated with the southward flowing Circumpolar Deep Water (CDW), its upwelling into the mixed layer, conversion into lighter Antarctic Intermediate Water (AAIW), followed by the AAIW subduction from the mixed layer into the oceanic interior. It can be seen from the figure that this circulation cell depends qualitatively on the model resolution. Essentially, in the two coarsest resolution model versions there are significant ($\approx$ 10 Sv) diapycnal fluxes between about 40°-50°S (Fig. 4.1a,b). These diapycnal fluxes allow for a formation of closed Deacon cells despite the use of potential density as the

vertical coordinate, rather than depth. Qualitatively similar, but weaker diapycnal fluxes ($\approx$ 5 Sv) forming a closed Deacon cell in density space have been reported by *Drijfhout* (2005) (bottom panel in his Fig. 10) in an eddy-permitting model.

At resolutions of 1.8°×3.6° and 0.6°×1.2°, the zonal mean clockwise Southern Ocean overturning is essentially decoupled from, or only weakly coupled to the rest of the world ocean (Figs. 4.1a,b; cf. Figs. 6b and 6d in *Gnanadesikan et al.* (2006). In contrast, as the model resolution increases, the Deacon cell becomes much weaker, barely appearing (as a closed cell) in the model version with the highest resolution employed (Fig. 4.1d), i.e. at 0.2°×0.4°. At this resolution, the CDW upwells adiabatically into the mixed layer (around 60°S and along about $\sigma_3 = 41.7$) and, after being transformed into AAIW, it outflows from the mixed layer (around 40°S and between about $\sigma_3 = 39.5$ and 40.5) and flows northward also near-adiabatically. Hence, as the model resolution increases, the zonal mean circulation associated with the upwelling of CDW and outflow of AAIW tends to follow isopycnals (Fig. 4.1c,d), thereby more effectively connecting the Southern Ocean to the rest of the world ocean.

The weaker coupling between the Southern Ocean MOC and the rest of the ocean seen in the coarse resolution model versions implies that light-to-dense water transformation in the North Atlantic, and the associated formation of NADW, is mostly compensated for by dense-to-light water conversion at low-latitudes (Fig. 4.2a). *Hirst and McDougall* (1998), using a 1.6°× 2.8° model, also simulate such an extreme situation for their MOC in latitude-density space (see their Figs. 4 and 5). Similar to the UVic ESCM, the *Hirst and McDougall* (1998) model uses the *Bryan and Lewis* (1979) profile to represent vertical diffusivity, K_v, with values at the base of the pycnocline of about 0.4×10^{-4} m^{2}s^{-1}. Using the advective-diffusive scaling (i.e. $A\ w = A\ K_v/h$, with A and h being, respectively, the area of low latitude ocean and mean depth of pycnocline) such K_v values can account for the deep water upwelling through the low-latitude ocean of the order of 10 Sv (with $A = 2.5\times10^{14}$m^2, $h = 10^3$m and

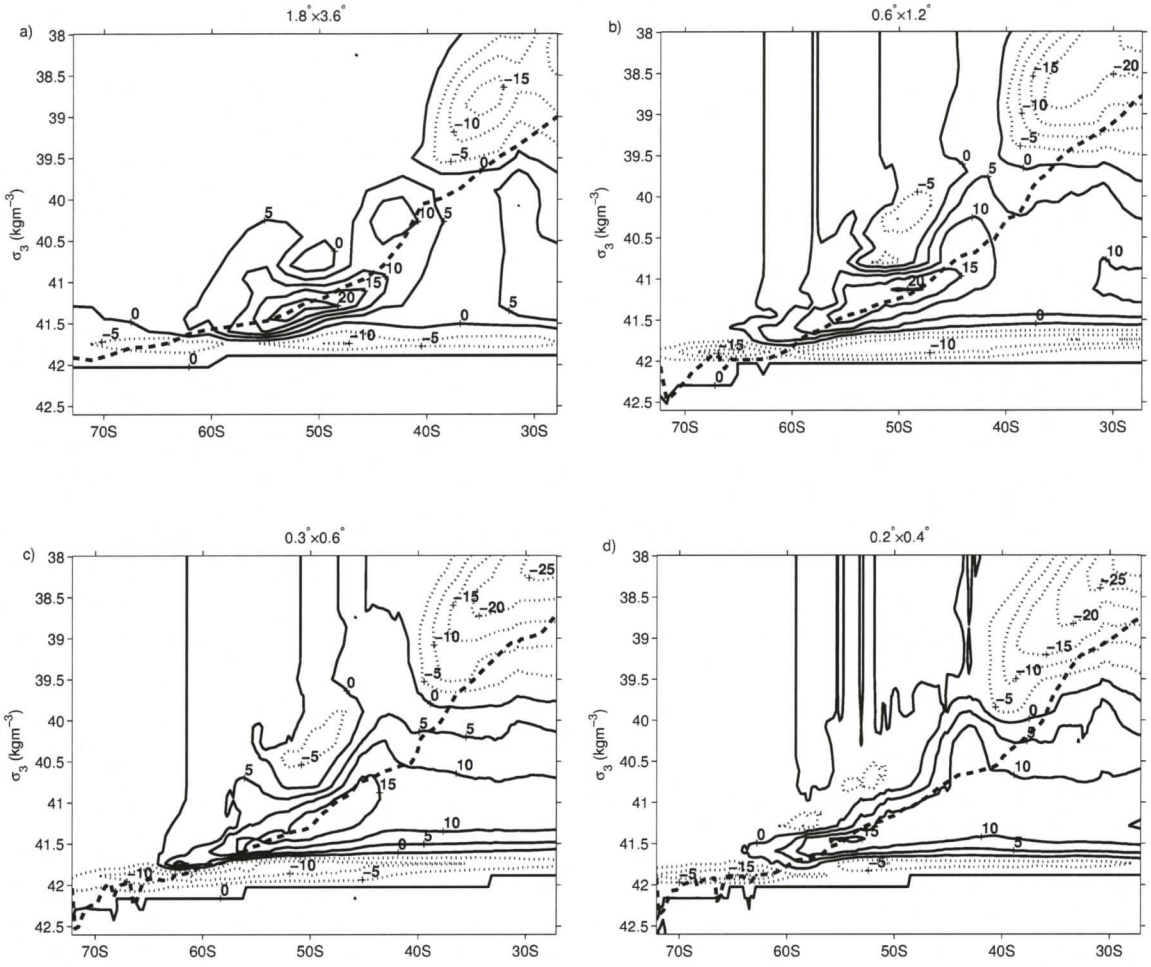

Figure 4.1: Southern Ocean Ψ_{RES} in the control state of the simulations. (a-d) correspond to horizontal resolutions of $1.8°\times3.6°$, $0.6°\times1.2°$, $0.3°\times0.6°$ and $0.2°\times0.4°$, respectively. Streamlines (5 Sv contour intervals) are plotted as a function of potential density referenced to 3000 m depth (σ_3). Solid lines (positive values) and dotted lines (negative values) indicate clockwise and counter-clockwise flow, respectively. The thick dashed line is a proxy for the maximum density of the mixed layer.

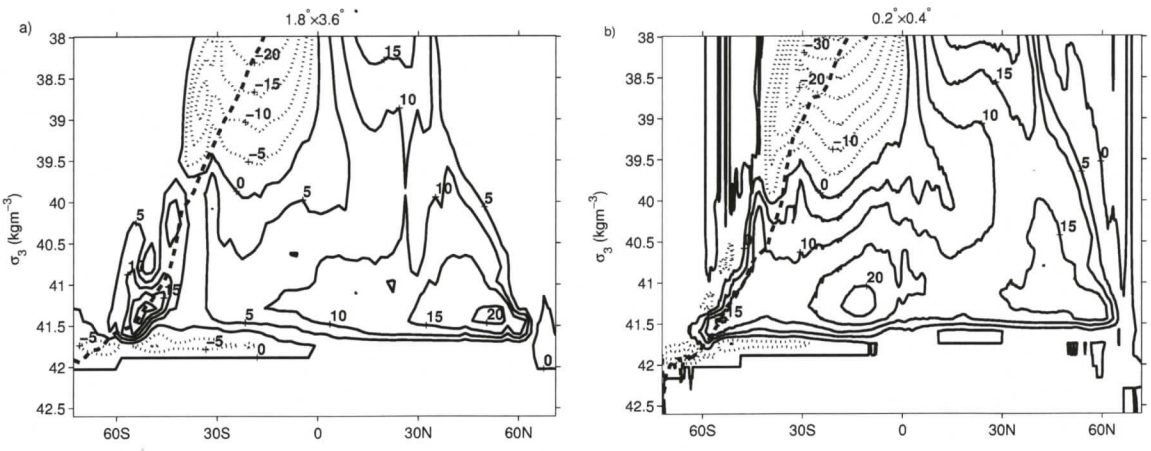

Figure 4.2: Ψ_{RES} for the Global Ocean in the control state at (a) 1.8°×3.6° and (b) 0.2°×0.4°. Plotted in the same manner as Fig. 4.1.

K_v=0.4×10^{-4} m^{2}s^{-1}, $A\ w$ = 10 Sv). In contrast, the MOC simulated by the high resolution model versions has the tendency for a more adiabatic circulation of NADW in the interior (Fig. 4.2b), so that about 2/3 of NADW forming in the northern North Atlantic (10 Sv out of 15 Sv) upwells in the Southern Ocean. (Note that the closed overturning cell centered near 15°S and σ_3 = 41.3 in Fig. 4.2b is predominately a feature of the Indian Ocean circulation.) In the high resolution models, the tendency for a near-adiabatic residual circulation in the interior is established despite the use of the same profile for vertical diffusivity (and the same criteria for convective mixing) as in the coarse resolution models. This implies that, as the resolution increases the overturning circulation becomes less sensitive to the representation of some subgrid scale processes. As a result, despite the use of relatively large values for K_v in the pycnocline, the NADW tends to upwell less through the low-latitude oceans, and more in the Southern Ocean. This may not always be easy to deduce from simple, scaling-based models of the global ocean overturning circulation, such as for example that of *Gnanadesikan* (1999).

To separate the contributions to Ψ_{res} arising due to the mean and eddy-induced components of the circulation, the following streamfunction is introduced (e.g, *Döös*

et al. (2008, 2009)):

$$\overline{\Psi}(y,\sigma_3) = \oint \int_{-H(x,y)}^{\overline{z}(x,y,\sigma_3)} \overline{v}(x,y,\overline{z}) d\overline{z} dx, \tag{4.2}$$

where time averaging is performed first, so that $\overline{v}(x,y,\overline{z})$ is the averaged in time meridional velocity binned into the (varying only in space) σ_3 surfaces, $\overline{z}(x,y,\sigma_3)$. Then, the eddy contribution to the residual streamfunction can be estimated as follows (e.g, *Döös et al.* (2008, 2009)):

$$\Psi^* = \Psi_{res} - \overline{\Psi}. \tag{4.3}$$

Calculated this way, the eddy-induced streamfunction in the $0.2°\times0.4°$ base-line model is shown in Fig. 4.3a. For comparison, shown in Figs. 4.3b,c are the eddy-induced streamfunctions corresponding to the $0.2°\times0.4°$ model versions with reduced viscosity, as described in section 4.2. The eddy-induced flow has a strong diapycnal component, with much of it confined to the mixed layer. With decreasing viscosity, the rate of eddy-induced overturning increases and it tends to penetrate to denser water classes. For comparison, Fig. 4.3d presents the overturning in the $1.8°\times3.6°$ model due to the GM90 eddy-induced velocity. The streamfunction induced by the parametrized eddies resembles those induced by the permitted eddies in that its maximum is positioned between 50°-60°S, albeit it is weaker (its strength depends on the value imposed for the coefficient of layer thickness diffusivity in the GM90 mixing scheme). In addition, the permitted eddies thus defined (i.e., as deviations from the annual mean state) can induce strong recirculating flows within the mixed layer (Fig. 4.3a-c), which are absent or much weaker than when the eddies are parametrized (Fig. 4.3d). Part of the reason for this is that, as noted, the "eddies" defined as deviations from a mean state obtained by averaging over one or several years are expected to include seasonal variability.

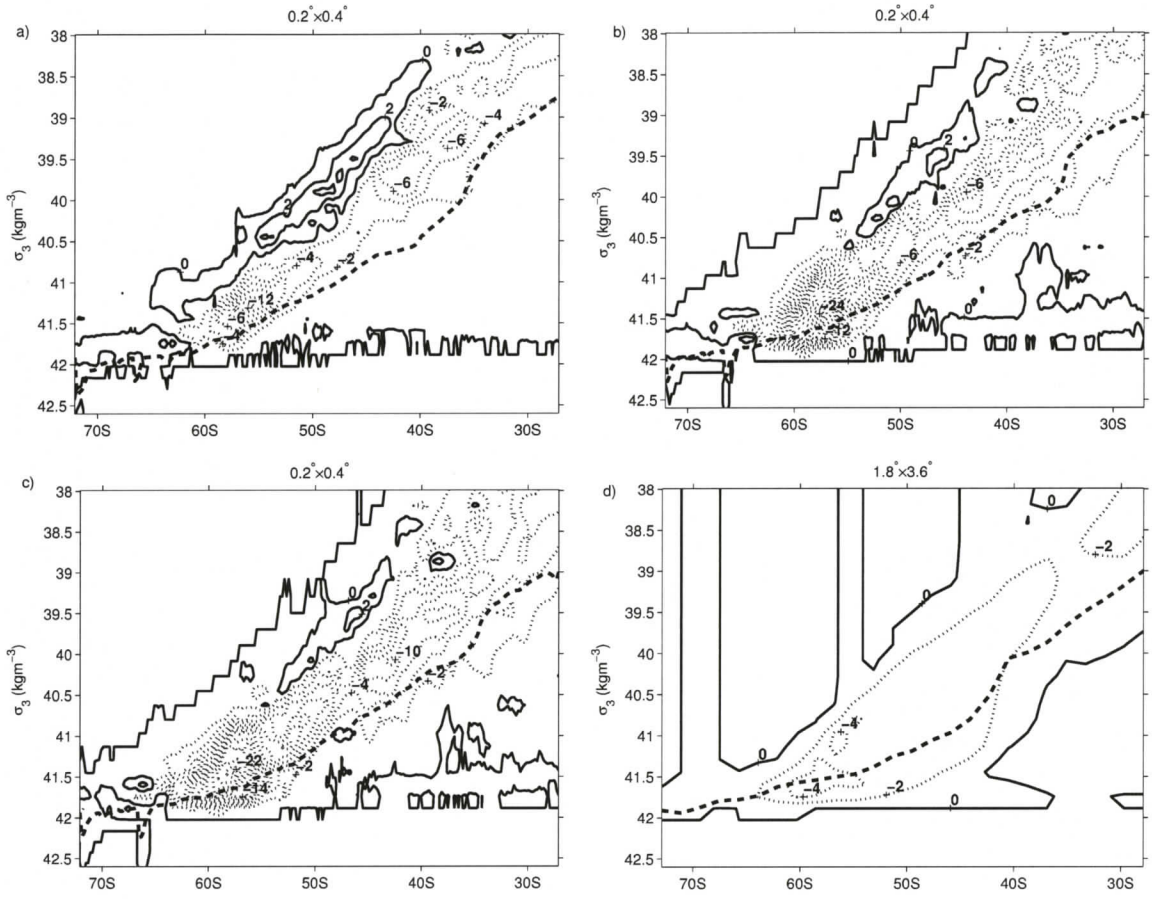

Figure 4.3: (a) Resolved Ψ^* for the Southern Ocean in the control state of the base-line $0.2°\times0.4°$ model ($A_M = 1.5\times10^4\ m^2/s$). (b-c) Resolved Ψ^* at $0.2°\times0.4°$ with A_M reduced to $10^3\ m^2/s$ and $2\times10^2\ m^2/s$, respectively. (d) The GM90 Ψ^* at $1.8°\times3.6°$. Plotted in the same manner as Fig. 4.1, except with 2 Sv contour intervals.

The impact of the seasonal variability can be reduced by noting that a more appropriate averaging operator in Eq. 4.2 would be a low-pass operator which would allow the mean variables to evolves with time (*McDougall and McIntosh* 1996). Replacing the long-term averaging in Eq. 4.2 by an averaging for each of the four seasons, the eddy cells in the mixed layer are strongly suppressed and the streamfunctions induced by the permitted eddies (Fig. 4.4a-c) more closely resemble that induced by the parametrized eddies (Fig. 4.4d). Both the permitted and the parametrized eddies induce closed overturning cells extending below the mixed layer in the Southern Ocean, between about 50°-60°S. This is consistent with previous studies (e.g., see Fig. 6b in *Hirst and McDougall* (1998); Fig. 4c in *Speer et al.* (2000a); Fig. 4 in *Saenko et al.* (2005); see also *Gent et al.* (1995), and is also in general agreement with a recent simulation based on an eddy-resolving (1/12°) model *Lee et al.* (2007); see their Fig. 5b). Differences between the seasonally and annually averaged eddy-induced overturning circulations are predominately found within the mixed layer; precisely where the use of GM90 parametrization is most questionable, and where the net effect of GM90 on the overturning depends on isopycnal slope tapering schemes (see *Danabasoglu et al.* (2008)).

4.3.2 Water Mass Transformation

If 1) the surface buoyancy flux dominates the diapycnal mixing within the mixed layer, 2) below the mixed layer the diapycnal mixing is weak, and 3) internal sources of buoyancy are negligible, then within the outcropping isopycnals the residual overturning circulation can be estimated using only the surface buoyancy flux (see Appendix B). This idea was originally proposed by *Walin* (1982) for the circulation associated with surface heat flux, and has been further elaborated in a number of more recent studies (e.g., *Iudicone et al.* (1997)). Essentially, the net mass transport in the direction of increasing buoyancy within the mixed layer (i.e. a conversion from dense water to lighter water) would be favoured by a buoyancy gain at the

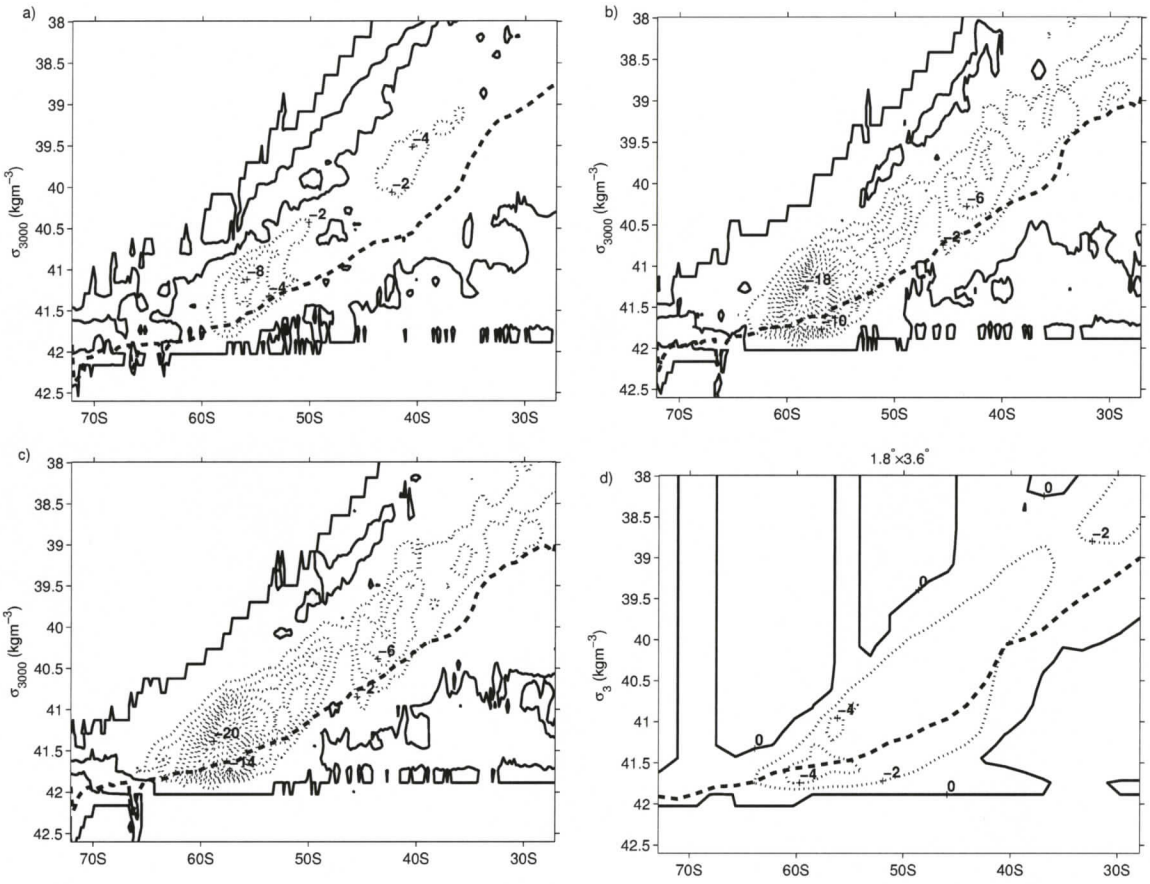

Figure 4.4: (a) Resolved Southern Ocean Ψ^* (2 Sv contours) in the base-line $0.2°\times0.4°$ model ($A_M = 1.5 \times 10^4\ m^2/s$) calculated with a seasonal time average operator. (b-c) Same as (a) but with with A_M reduced to $10^3\ m^2/s$ and $2 \times 10^2\ m^2/s$, respectively. (d) The GM90 Ψ^* at $1.8°\times3.6°$.

surface, whereas a conversion from light water to denser water would be favoured by a buoyancy loss.

Some of the above assumptions may not always be easy to justify. For example, the diapycnal mixing in the near surface ocean, such as that arising due to the diabatic component of mesoscale eddy buoyancy flux, may not be weak (e.g. *Radko and Marshall* (2004)). In this regard, the question aimed to be addressed here is how much of the cross-isopycnal volume transport in the Southern Ocean mixed layer, particularly within the density ranges of the CDW-to-AAIW conversion, can be attributed to the surface buoyancy flux.

The quantity which is estimated in practise is the so-called transformation rate from one buoyancy class to another (e.g., *Speer et al.* (2000a,b)), given by

$$\mathcal{F}(b') = \int_{year} dt \int\int_{area} -B_o \, dxdy \, \delta[b(x,y,t) - b'], \tag{4.4}$$

with the δ function permitting sampling of the surface buoyancy flux, B_o, only for surface water of buoyancy b. The surface buoyancy flux is given by,

$$B_o = -\frac{g\alpha}{\rho_o C_w} H(x,y,t) + \frac{g\beta S_o}{\rho_o} W(x,y,t), \tag{4.5}$$

where g is the gravitational constant, α = - $\rho^{-1}(\partial\rho/\partial T)_{p,s}$, $\beta = \rho^{-1}(\partial\rho/\partial S)_{p,T}$, C_w is the specific heat of water, ρ_o and S_o are the reference density and salinity, H and W are, respectively, the net heat and freshwater fluxes. The transformation rate estimated this way combined with both the advective and diffusive components of the buoyancy transport comprises the total steady-state buoyancy budget between isopycnals (*Garrett et al.* 1995, *Speer et al.* 2000a,b); see also Appendix B.

As the first step, the model-derived transformation rates in the of Southern Ocean are compared with a transformation estimate based on observations. In the latter case, a dataset is used (hereafter referred to as NCEP_LEV) which comprises the

NCEP50 reanalysis model surface fluxes (*Kistler et al.* 2001) and the Levitus sea surface climatology (*Levitus et al.* 1994). The main focus is on the model version with the highest resolution where, as shown in Figure 4.1d, the cross-isopycnal volume flux in the mixed layer can serve as a good proxy for the near-adiabatic interior circulation associated with the upwelling of CDW and subduction of AAIW. However, it is also of interest to compare the transformation rates for all four UVic ESCM simulations.

The UVic ESCM transformation rates have similar profiles in all four simulations and three principal density classes of transformation are identifiable (Fig. 4.5a). (Note that σ_3 is used in this and all other figures showing transformation rates, which is motivated by the desire to be able to directly compare $\mathcal{F}(\sigma_3)$ with the overturning circulation where σ_3 is also used; only small differences are found in the shape of the transformation curves when using σ_0 instead of σ_3). These density classes correspond to the surface waters of the three cells found in the MOC (Fig. 4.1). Surface water in the highest density class ($\sigma_3 > 41.7$), corresponding to polar cell waters, are gaining density in the UVic ESCM simulations. Separating $\mathcal{F}$ into haline and thermal components (Fig. 4.5b) demonstrates that the formation of Antarctic Bottom Water (AABW) is dominated by surface salt fluxes resulting from brine rejection during sea ice formation. Transformation in this density class for the NCEP_LEV dataset is zero because the reanalysis data does not explicitly include brine rejection and also because in the high latitudes the Levitus data is dominated by summer-time observations. In all five datasets, both haline and thermal forcings play a role in transforming the surface water of the CDW/AAIW cell ($39.5 < \sigma_3 < 41.7$). In the UVic ESCM simulations the lightening of this subpolar cell surface waters by haline forcing dominates a weak density gain by heat loss in the $40.8 < \sigma_3 < 41.7$ density range, while both heat gain and salt loss are responsible for the lightening in the $39.5 < \sigma_3 < 41$ density range. Similar results are found for NCEP_LEV data with the exception of greater haline forcing between $39.8 < \sigma_3 < 41.3$, which increases the net

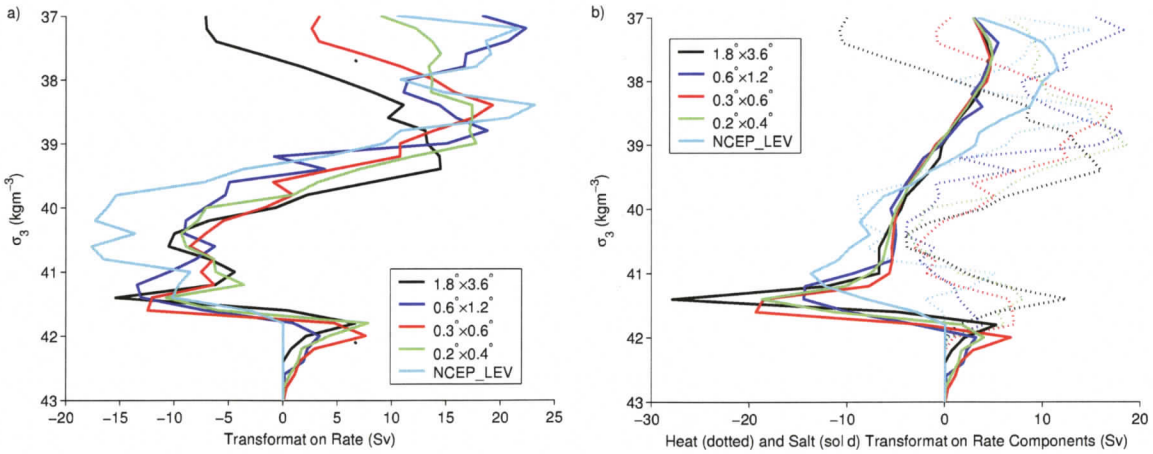

Figure 4.5: Residual transformation rates ($\mathcal{F}$) of Southern Ocean water masses for each of the UVic ESCM simulations as well as a dataset comprised of NCEP reanalysis surface fluxes and Levitus sea surface climatology. (a) presents the total transformation rates and (b) separates it into surface heat (dotted lines) and salt (solid lines) flux components.

transformation rate over this density range relative to the UVic ESCM simulations. The gain in density of subtropical cell water ($\sigma_3 <$ 39.5) is primarily the result of surface heat loss in all five datasets. Greater thermal buoyancy gain is found between ($39.8 < \sigma_3 < 41$), but otherwise thermal forcing in NCEP_LEV dataset is within the range of the UVic ESCM simulations.

As noted, to the extent that the surface buoyancy flux dominates the eddy diapycnal mixing within the mixed layer, the residual cross-isopycnal volume flux within the layer, $\Psi_{res|z=-h_m}$, is expected to be compatible with $\mathcal{F}$. Qualitatively, within the density classes of the CDW-to-AAIW conversion ($39.5 < \sigma_3 < 41.7$) which is of major interest here, all models show such a compatibilty (Fig. 4.6). The focus, however, is on the $0.2° \times 0.4°$ model, where eddies are permitted and where the diapycnal flux within the mixed layer is a good proxy for the near-adiabatic circulation of CDW/NADW and AAIW in the interior. From Figure 4.6d, it can be seen that for this density range, except perhaps at its upper limit, the volume transport within the mixed layer simulated by the $0.2° \times 0.4°$ model is well captured by the corresponding transformation rate. For the densest waters within this range (around $\sigma_3 = 41.2$),

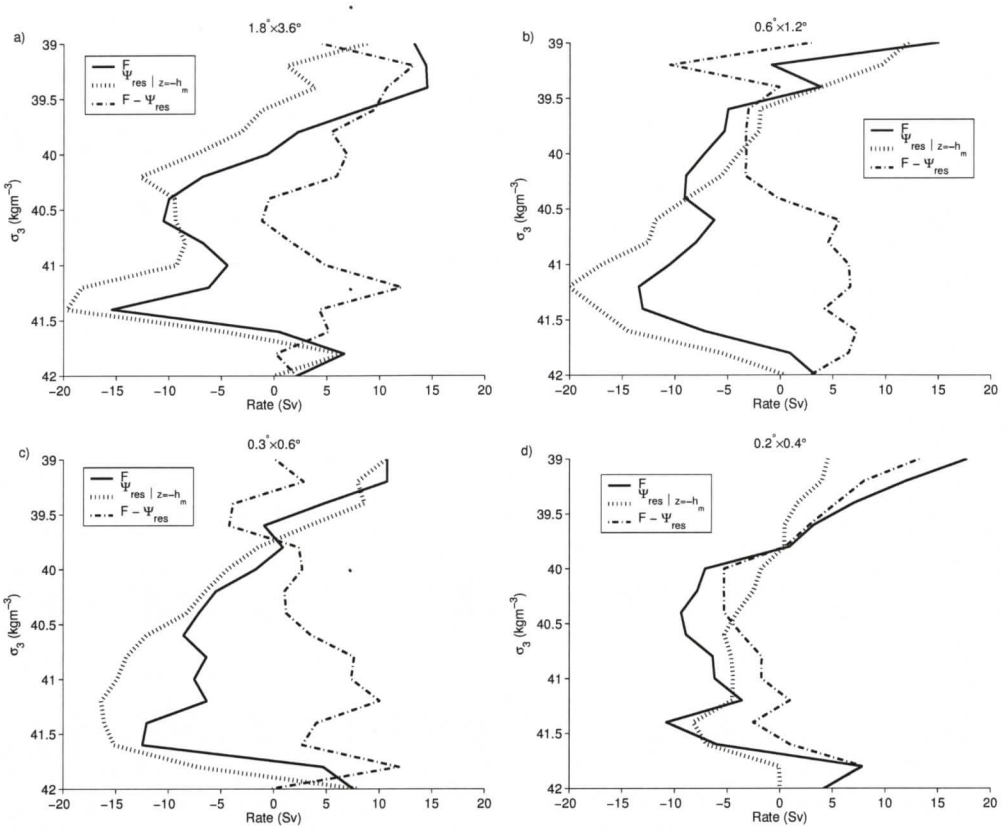

Figure 4.6: Residual transformation rate ($\mathcal{F}$) of CDW/AAIW water masses along with the residual transport through the base of the mixed layer ($\Psi_{res|z=-h_m}$) in the control simulations. Note that in these plots negative $\Psi_{res|z=-h_m}$ values represent northward transport.

only about 50% of the cross-isopycnal volume transport is accounted for by the surface buoyancy flux (Fig. 4.6d). This suggests that the buoyancy flux arising due to the diabatic component of the (permitted) mesoscale eddies can, for some density classes, be of the same order as the surface buoyancy flux and, hence, cannot be neglected. Thus, it may not always be possible to infer $\Psi_{res|z=-h_m}$ from $\mathcal{F}$, consistent with *Treguier et al.* (2007). However, for some density classes, $\mathcal{F}$ can be a good proxy for $\Psi_{res|z=-h_m}$ (Fig. 4.6d) and, hence, for the corresponding near-adiabatic circulation in the interior.

Can this be useful? First, it takes time for the interior flows to come into equilibrium with the surface boundary conditions and, second, a change in the circulation

could feed back on surface fluxes. Nonetheless, these results suggest that in some cases, it might be possible to infer the interior circulation from the surface buoyancy flux. Moreover, one may hope to diagnose changes in the circulation in response to a changing climate which, at steady state, are expected to be largely compatible with changes in the surface buoyancy flux. However, such a compatibility, as shown next, may not always be insured at the transient stage of the circulation-flux adjustment.

4.4 Projected 21^{st} Century Response

In this section, projected 21st century changes in the circulation associated with the upwelling of CDW and its conversion to AAIW are briefly considered. An expectation is that this conversion may increase for two reasons. First, the wind stress, which is imposed in the models to correspond to that projected for the 21st century (*Fyfe et al.* 2007), increases over the Southern Ocean, particularly its zonal component. Hence, the Eulerian mean overturning should also increase; this could, at least in part, be compensated by the eddy-induced return flow. Second, with the increasing concentration of greenhouse gases, the buoyancy gain in the subpolar oceans, including in the Southern Ocean, is expected to increase both due to the associated warming and enhanced precipitation. Again, this could be partly compensated by the diabatic eddy fluxes. Furthermore, as the concentration of greenhouse gases increases and the upper ocean warms up more than the deeper ocean, it is expected that the oceanic stratification will also generally increase. This has a potential to influence low-latitude upwelling of deep water and the eddy-induced transport. Overall, how (and if) all these and other changes would translate into the changes in the overturning circulation is not easy to foresee.

The focus is on the circulation projected by the two model versions with higher resolution. Since running the $0.2°\times0.4°$ model is computationally quite expensive, it was only integrated to obtain the projection to the year 2080. Changes in the

overturning circulation are evaluated at year 2080 to facilitate a fair comparison between the simulations. Note, however, that the Southern Ocean wind stress is projected to continue to strengthen beyond 2080 (*Fyfe et al.* 2007, *Saenko* 2007b), so that a change in the overturning circulation by 2080 may differ from that projected by the century end, although one would not expect qualitative differences.

According to the $0.3°\times0.6°$ model, the MOC corresponding to the density range of main interest here (roughly $39.5 < \sigma_3 < 41.7$) does not slow down (Fig. 4.7a). Rather, by the year 2080 it is projected to intensify (Fig. 4.7c). This intensification is not confined to the southern hemisphere; rather, on these time scales it is carried into the Northern Hemisphere (not shown). However, the amplitude of this cross-equatorial penetration of the overturning circulation anomaly from the south to the north may depend on the model's ability to capture the adjustment processes due to coastal and equatorial Kelvin waves. Further discussion of this important process is beyond the scope of this study (but see *Johnson and Marshall* (2004)). The $0.2°\times0.4°$ model also projects an intensification of the Southern Ocean MOC (Figs. 4.7b,d).

Further insight can be obtained by considering the projected changes in the transformation rates that, together with the corresponding mixed layer transports, are shown in Fig. 4.8. Since this deals with transient changes in the circulation, these should not be expected to be as compatible with the transformation rates as they are in the control simulations. Nevertheless, this study has demonstrated that for many density classes at steady state, the circulation implied by $\mathcal{F}$ is compatible with $\Psi_{res|z=-h_m}$ (Fig. 4.6). Therefore, it seems reasonable to expect that at near steady state, there would be a similar compatibility between $\mathcal{F}$ and $\Psi_{res|z=-h_m}$ in the future.

According to the $0.3°\times0.6°$ model, both $\mathcal{F}$ and $\Psi_{res|z=-h_m}$ increase by more than 10 Sv around $\sigma_3 = 40$ (Fig. 4.8c) by year 2080. Projected changes in $\mathcal{F}$ and $\Psi_{res|z=-h_m}$ by the $0.2°\times0.4°$ model indicate an increase around $\sigma_3 = 41$ by year 2080 (Fig. 4.8d). Neither model shows a decrease in CDW-to-AAIW conversion, and both simula-

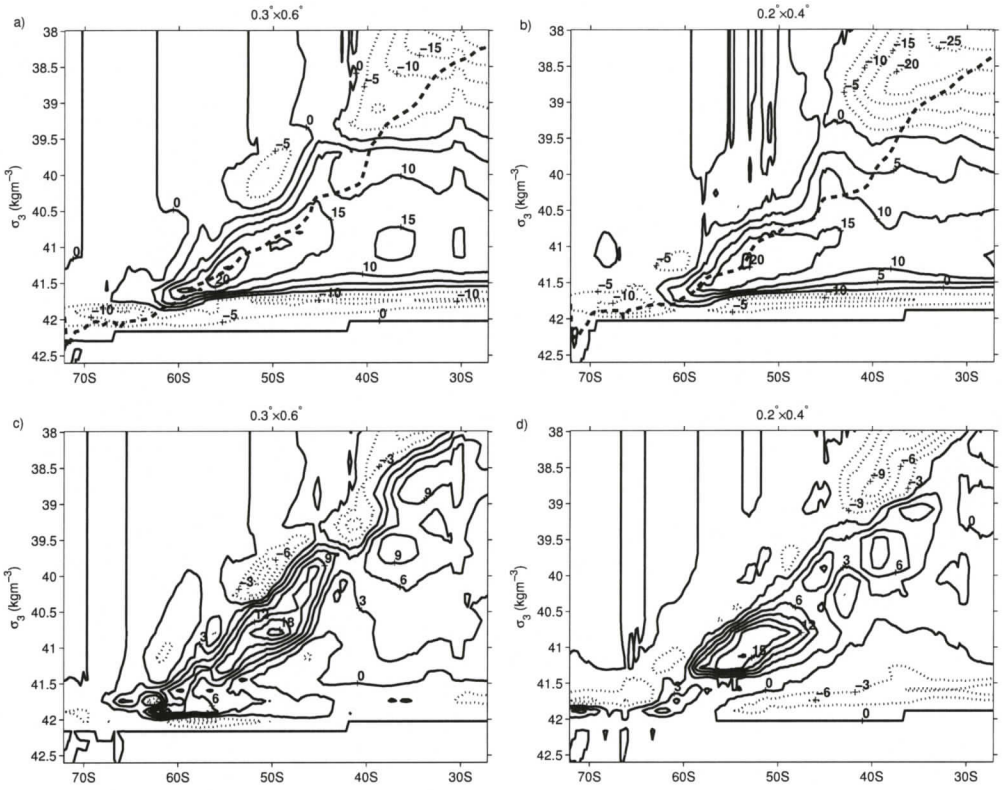

Figure 4.7: (a) Year 2080 Ψ_{RES} at 0.3°×0.6° and (b) at 0.2°×0.4° (5 Sv contour intervals). (c) and (d) show Ψ_{RES} anomalies (3 Sv contour intervals) relative to the year 1900 control state.

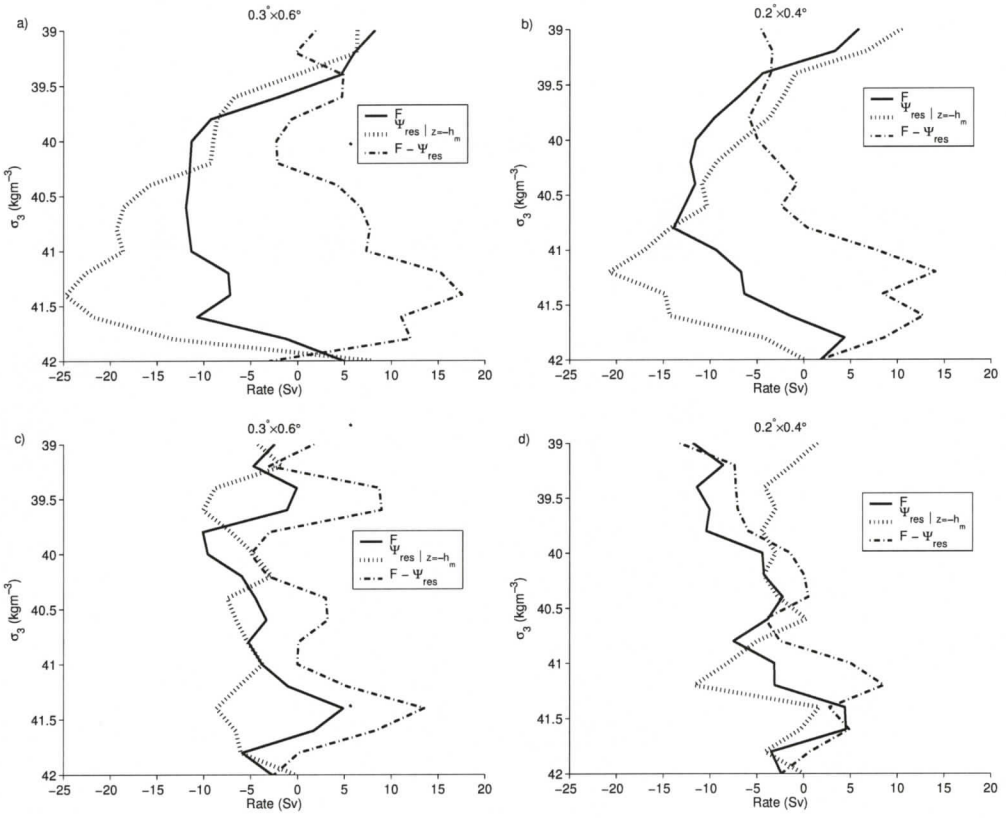

Figure 4.8: (a) and (b) show $\mathcal{F}$ and $\Psi_{res|z=-h_m}$ in year 2080 at $0.3°\times0.6°$ and $0.2°\times0.4°$, respectively. (c) and (d) show anomalies relative to year 1900.

tions show that much of the increase in $\Psi_{res|z=-h_m}$ is due to the local recirculation (Fig. 4.7c,d), with only a fraction of it extending further north. However, given the tendency for a near adiabatic circulation of deep water under the near steady conditions (Fig. 4.1d), the projected local diabatic recirculation (Fig. 4.7b,d) should be expected to decrease on longer time scales, thereby increasing the positive overturning circulation anomaly penetrating to the Northern Hemisphere.

4.5 Conclusions

Climate models are extensively employed for studying the climate variability associated with changes in the ocean MOC. The bulk of the previous work has focused on the northern North Atlantic, where a conversion from light to dense waters and the associated formation of NADW can be sensitive to surface buoyancy input. However, the MOC is also expected to be influenced by dense to light water conversion processes, as occurs in the Southern Ocean – a region of strong mesoscale eddy activity. Whereas a great deal of the earlier work in this area has been based on coarse-resolution models with mesoscale processes being heavily parametrized, the Southern Ocean branch of the MOC and its response to changes in the climate could be quite sensitive to the representation of mesoscale effects in models.

Here, four versions of the same climate model have been employed, with horizontal resolutions ranging from $1.8°\times3.6°$ to $0.2°\times0.4°$. As the resolution increases and, in particular, as eddy effects become less parametrized, the deep water forming in the North Atlantic tends to upwell more in the Southern Ocean and less in the low-latitude oceans. At the highest resolution employed ($0.2°\times0.4°$), out of 15 Sv of diapycnal light-to-dense water conversion in the north (around 60°N and across isopycnals between $40.5 < \sigma_3 < 41.5$), about 10 Sv upwells in the Southern Ocean. In contrast, in the coarse resolution model versions, most of the NADW upwells at low-latitudes, so that the Southern Ocean becomes, on zonal mean, less coupled with

the rest of the ocean. This is despite the use of the same profile for vertical diffusivity in all four model versions, with values that (potentially) allow for as much as 10 Sv of dense-to-light water transformation through the low-latitude pycnocline.

It is found that as the resolution increases, the interior residual circulation within the density range of CDW-to-AAIW conversion becomes more adiabatic. However, both the permitted eddies in the highest resolution model versions and the eddies parametrized using the GM90 scheme induce closed overturning cells in the Southern Ocean, with maxima centred between 50°-60°S. This is in agreement with a recent simulation based on an eddy-resolving (1/12°) model *Lee et al.* (2007). In addition, while the relation between surface buoyancy flux and meridional streamfunction in the Southern Ocean has been questioned by *Treguier et al.* (2007), this study finds that for many density classes the so-called transformation rate is a good proxy for the interior circulation, although in general the diapycnal eddy fluxes in the mixed layer cannot be neglected.

Finally, two model versions with higher resolution are used to project future changes in the MOC in response to changes in the climate induced by accumulation of greenhouse gases in the atmosphere. For the latter, the IPCC SRES scenario A2 is used. Since the atmospheric component of the model is rather simple, the corresponding changes in the wind stress are imposed. These are derived from a set of climate change projections based on fully-coupled models.

At least two factors are of major importance to the Southern Ocean MOC response. The first is related to the projected strengthening in the Southern Ocean zonal wind stress. This tends to intensify the Eulerian mean component of the overturning, which can be partly or totally offset by strengthening of the eddy-induced overturning. Second, the projected stronger buoyancy input at the surface in the subpolar oceans, while favouring a reduction of light-to-dense water transformation in the northern North Atlantic, favours an intensification of the reverse process in

the Southern Ocean. The overall effect of these changes on the upper ocean MOC in the warmer climate is difficult to foresee. However, based on these model results, it can be concluded that on a century-long time scale, the circulation associated with the CDW-to-AAIW conversion is more likely to intensify, rather than to slow down, in general agreement with discussions presented in *Toggweiler and Russell* (2008), *Saenko* (2007b). This should be expected to eventually affect the rate of light-to-dense water conversion in the Northern Hemisphere and the associated flow of NADW in a warmer climate. In particular, increasing oceanic resolution from 1.25° to 1/3°, *Roberts et al.* (2004) found a less pronounced weakening of the meridional overturning and heat transport in the Atlantic in their climate model in response a 2% yr^{-1} increase in CO_2. More recently, *Delworth. and Zeng* (2008) simulated an intensification of the Atlantic MOC in response to a change in the Southern Ocean wind stress similar to that imposed in this study, but using the GFDL fully-coupled model and keeping other forcings unchanged.

Chapter 5

The Southern Ocean Temperature and Antarctic Circumpolar Current Response to Poleward Intensifying Winds

5.1 Introduction

The size, remoteness, and inhospitable environment of the Southern Ocean has made observational data relatively scarce, resulting in higher uncertainty estimates than found in other ocean basins (e.g. *Levitus et al.* (2000)). Despite these challenges, observations from the past few decades indicate that a section of the Southern Ocean between 40°-60°S has been warming at nearly twice the rate of the global ocean over the top 1000 m. (*Gille* 2002, *Aoki et al.* 2003, *Gille* 2008). Observations concurrently show a poleward shift and strengthening of southern hemisphere westerly winds, identified as a shift in the Southern Annual Mode (SAM) towards a higher index state (*Thompson and Solomon* 2002). These changes in the southern winds appear to be due to anthropogenic forcing, with increasing atmospheric concentrations of both ozone depleting (*Gillett and Thompson* 2003) and greenhouse gases (*Fyfe* 2006) identified as playing critical roles. General circulation models (GCMs) are remarkably consistent in predicting a significant amplification of this SAM signal throughout

the next century (*Fyfe and Saenko* 2006). Southern Ocean sea surface temperatures (SST) and the ACC are known to respond to SAM variability on interannual and seasonal timescales (*Hughes et al.* 2003, *Ciasto and Thompson* 2008). The link between poleward intensifying winds and enhanced Southern Ocean warming and ACC transport is a fundamental question of 21^{st} century global climate change and subject of much debate.

The oceanic temperature response in coarse resolution GCMs to poleward intensifying winds through the 21^{st} century is a warming of surface to mid-depth waters along the northern edge of the ACC and a cooling at higher and lower latitudes (*Fyfe et al.* 2007, *Sen Gupta and England* 2006). This response is primarily due to an enhanced northward Ekman transport and changes in Ekman pumping. Coarse resolution models also show an increase in ACC transport that approximately linearly follows the maximum windstress, and a poleward shift in its mean position (*Fyfe and Saenko* 2006). However, the ability of coarse resolution models to accurately capture the Southern Ocean response to poleward intensifying winds has been questioned (*Böning et al.* 2008). It has been argued that the ACC may exist in an eddy saturated state where an increase in the surface wind stress increases mesoscale eddy fluxes (*Meredith and Hogg* 2006). The enhanced eddies can transfer momentum to deep layers and generate fluxes that may compensate for the effects of Ekman transport and pumping anomalies, with little overall effect on the mean ACC (*Hallberg and Gnanadesikan* 2001). An enhanced meridional eddy heat flux could contribute to Southern Ocean warming (*Hogg et al.* 2008), as could the poleward displacement of distinct Southern Ocean frontal features (*Gille* 2008). Unfortunately, the ability of modern eddy-resolving models to accurately project long-term changes are limited by computational constraints that often require non-global spatial domains with idealized boundary conditions and short integration periods.

This study investigates the horizontal resolution dependence of the Southern

Table 5.1: Salient features of the Antarctic Circumpolar Current

Horizontal Resolution	1.8°×3.6°	0.6°×1.2°	0.3°×0.6°	0.2°×0.4°
Yr 1900 DPT (Sv)	115	195	210	175
Yr 2080 DPT Anoms. (Sv)	9.6	10.3	11.7	6.1
Yr 2080 Atlantic ACC Shift (°S)	1.22	1.31	1.34	0.76
Yr 2080 Indian ACC Shift (°S)	2.04	0.83	2.11	0.38
Yr 2080 Pacific ACC Shift (°S)	0.58	0.11	0.22	0.23
Yr 2080 Global ACC Shift (°S)	1.12	0.65	1.14	0.43

DPT refers to the maximum volume transport through Drake Passage. Poleward shifts in ACC position in response to poleward intensifying winds are determined by calculating the mean position of the mean ACC transport in each basin.

Ocean response to poleward intensifying winds through the 20th and 21st centuries. Changes in Southern Ocean temperature, sea ice thickness, meridional ocean eddy heat transport, and the ACC are evaluated.

5.2 Experimental Design

This study employs the same four base-line versions of the UVic ESCM described in section 4.2. While the control state drift of globally averaged ocean temperature in the higher resolution models is relatively small, there can be stronger trends in the temperature of specific regions. Model drift is accounted for in this study by differencing simulations forced with (i) increasing atmospheric CO_2 concentration concomitant with southern hemisphere surface wind anomalies from those forced with (ii) increasing CO_2 alone. Both the CO_2 (increases from 295 ppm at year 1900 to 830 ppm by 2100) and surface wind forcing is applied in the same manner as discussed in section 4.2. Computational constraints limits the period of the forcing simulations at 0.2°×0.4° to 1900-2080, while the three coarser resolution models are integrated to 2100.

5.3 Projected 21st Century Response

The Southern Ocean temperature response to the change in winds (Fig. 5.1) can be characterized as having more regional structure and local intense anomalies at higher resolution. The coarsest resolution (1.8°×3.6°) simulation has a diffuse and zonally uniform temperature response, with warming between roughly 40-55°S, and cooling at higher and lower latitudes. Much of the warming results from an increase in downward Ekman pumping that deepens isotherms, while a reduction in downward Ekman pumping north of roughly 40°S and an intensification of upward Ekman pumping south of about 60°S produces a shallowing of isotherms and cooling (*Fyfe et al.* 2007).

This general pattern of temperature response remains robust as the model resolution increases, and is in general agreement with observed anomalies during positive SAM events (*Ciasto and Thompson* 2008). However, at 0.6°×1.2° and 0.3°×0.6° resolutions the warming is intensified in a zonal band structure near 43°S in the Atlantic and Indian basins, with local anomalies as much as 3.5°C warmer than those of the 1.8°×3.6° simulation. At 0.2°×0.4° the warming signal is also most prominent in the Atlantic and Indian basins, with particularly intense local warming near the Brazil-Malvinas confluence, but there is no discernible zonal band structure. The three higher resolution models all have local regions of relatively large (> 1.5°C) cooling, particularly at midlatitudes in the Indian and Pacific basins. Patches of local cooling are increasingly interspersed with warming patches at a common latitude as the resolution increases into the eddy-permitting range.

The 2075-2080 mean ACC position (Fig. 5.1) is determined for each simulation by adding the difference in position between the two forcing scenarios (i.e. the poleward intensifying wind effect; see Section 2) to the control state ACC position. All four simulations show poleward migration of the ACC in the Atlantic and the western half

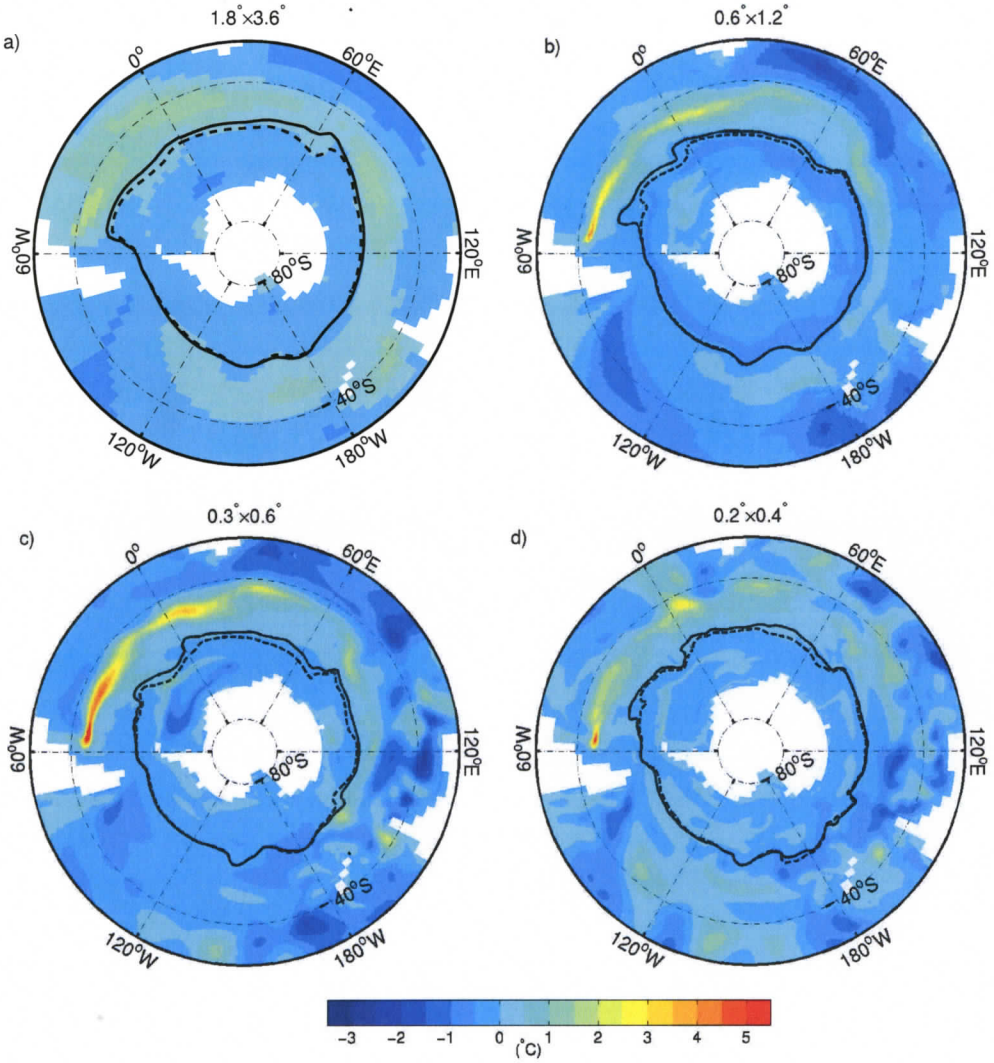

Figure 5.1: Frames (a-d) correspond to model horizontal resolutions of 1.8°×3.6°, 0.6°×1.2°, 0.3°×0.6°, and 0:2°×0.4°, respectively. (colour) Ocean temperature anomaly (°C) averaged over the upper 980 m and between years 2075-2080. (solid black line) Position of mean ACC transport in five year control state averages (year 1900) and between years 2075-2080 (dashed black line).

of the Indian basin, while only slight changes are found in the eastern Indian and Pacific basins. When averaged both globally and separately over individual basins (Table 5.1) the $1.8° \times 3.6°$ experiment tends to exhibit the largest poleward shift in ACC position, while the $0.2° \times 0.4°$ simulation exhibits the smallest. The reduced shift in ACC position at higher resolutions is likely due to the ACC being more constrained by higher resolution topography. An observational analysis by *Gille* (2008) indicates that the long-term Southern Ocean temperature trend is regionally consistent with a poleward displacement of temperature fronts in conjunction with the ACC, and that the shifting of fronts could account for most of the observed warming.

Near-surface Southern Ocean frontal features are evaluated with five year averages of meridional temperature gradients at 285 m depth, following the the *Belkin and Gordon* (1996) definition of the Subantarctic Front. Meridional temperature gradients in the $1.8° \times 3.6°$ control state (Fig. 5.2a) are relatively diffuse. In the $0.3° \times 0.6°$ control state (Fig. 5.2c) there are lengthy zonal bands of frontal structures (also true at $0.6° \times 1.2°$, not shown). The $0.2° \times 0.4°$ control state (Fig. 5.2e) has a more complex, filamented frontal structure and is the simulation that most approaches patterns found in observations (e.g. Plate 1c of *Hughes and Ashe* (2003), Fig. 5b of *Sallee et al.* (2008)). Increasing resolution clearly enhances the ability of the model to resolve the sharp meridional gradients that comprise the frontal bandings of the Southern Ocean.

Temperature gradient anomalies are generally weak at the end of the $1.8° \times 3.6°$ simulation (Fig. 5.2b). Strong anomaly dipole patterns are evident over the Atlantic and Indian basins at $0.3° \times 0.6°$ (Fig. 5.2d), with values that generally indicate a southward shift in frontal positions. This is in general agreement with available hydrographic observations, which identify a poleward movement of fronts in the Indian basin, an equatorward movement in the central Pacific, and a little meridional movement in the Indo-Pacific basin during positive SAM events (*Sallee et al.*

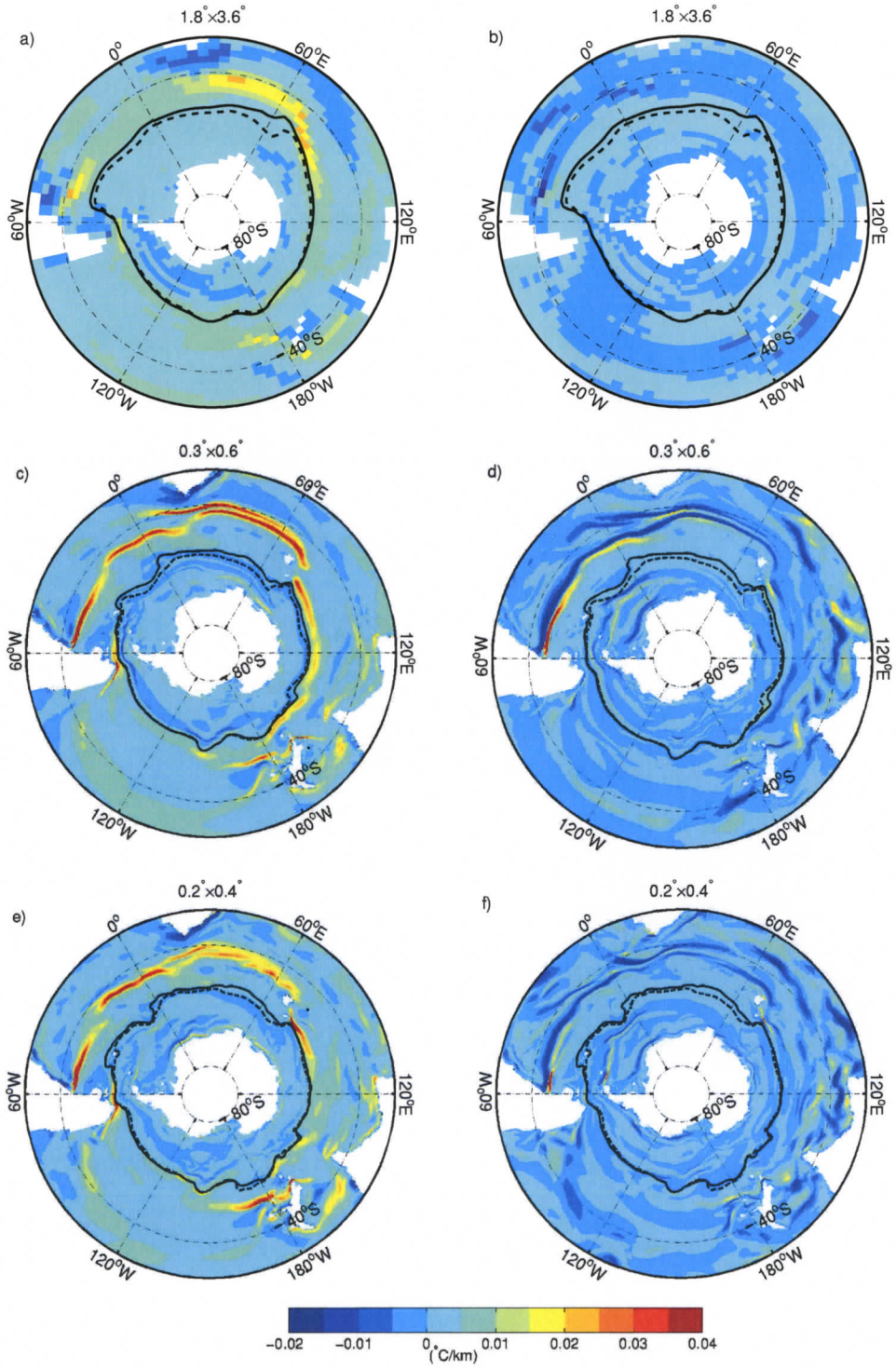

Figure 5.2: (colour) Meridional temperature gradients (°C km^{-1}) at 1.8°×3.6°, 0.3°×0.6° and 0.2°×0.4° at 285 m depth in five year control state averages (a,c,e) and gradient anomalies averaged over years 2075-2080 (b,d,f). (black lines) ACC position is plotted as in Fig. 5.1.

2008). A comparison between Fig. 5.1c and Fig. 5.2d reveals that the locations of intense warming at $0.3°\times0.6°$ tend to be co-located with poleward shifting temperature fronts and ACC positions (this is also true at at $0.6°\times1.2°$, not shown). Gradient anomaly dipoles are also evident at $0.2°\times0.4°$ (Fig. 5.2f), but they are generally weaker (excluding the Brazil-Malvinas confluence) and less zonally continuous than seen at $0.3°\times0.6°$. These results demonstrate that the southward migration of distinct frontal features is associated with a local intensification of Southern Ocean warming, in agreement with *Gille* (2008). Also note that the extensive frontal structures of the $0.6°\times1.2°$ and $0.3°\times0.6°$ simulations may be indicative of a relatively high viscosity, low diffusion regime in which the temperature response is especially sensitive to frontal shifts.

In a zonal and depth averaged view the general structure of the temperature response (Fig. 5.3a), with warming between roughly 40-55°S and cooling at higher and lower latitudes, remains robust as the model resolution increases. Note that both the $0.6°\times1.2°$ and $0.3°\times0.6°$ simulations exhibit more low latitude cooling, which is evidently due to Ekman upwelling of colder subsurface waters found in these simulations (not shown). In the $0.3°\times0.6°$ experiment, the distinct peak of amplified warming around 43°S clearly illustrates the strong effect of meridional shifts in temperature fronts. All models show a reduction in sea ice thickness south of 65°S in response to offshore Ekman transport. Note that, as the resolution increases into the eddy-permitting range, there is generally a significant reduction in the zonal mean cooling response south of 55°S, and a greater loss of sea ice thickness south of 65°S (Fig. 5.3b).

Figure 5.3c shows the zonal and depth integrated resolved eddy meridional heat transport of the two highest resolution models, along with the GM90 parametrized eddy heat transport of the two coarsest resolution models, averaged over the year 1900. Resolved eddy heat transports were calculated with the identity $\overline{\mathbf{v}'\theta'} = \overline{\mathbf{v}\theta} - \overline{\mathbf{v}}\,\overline{\theta}$

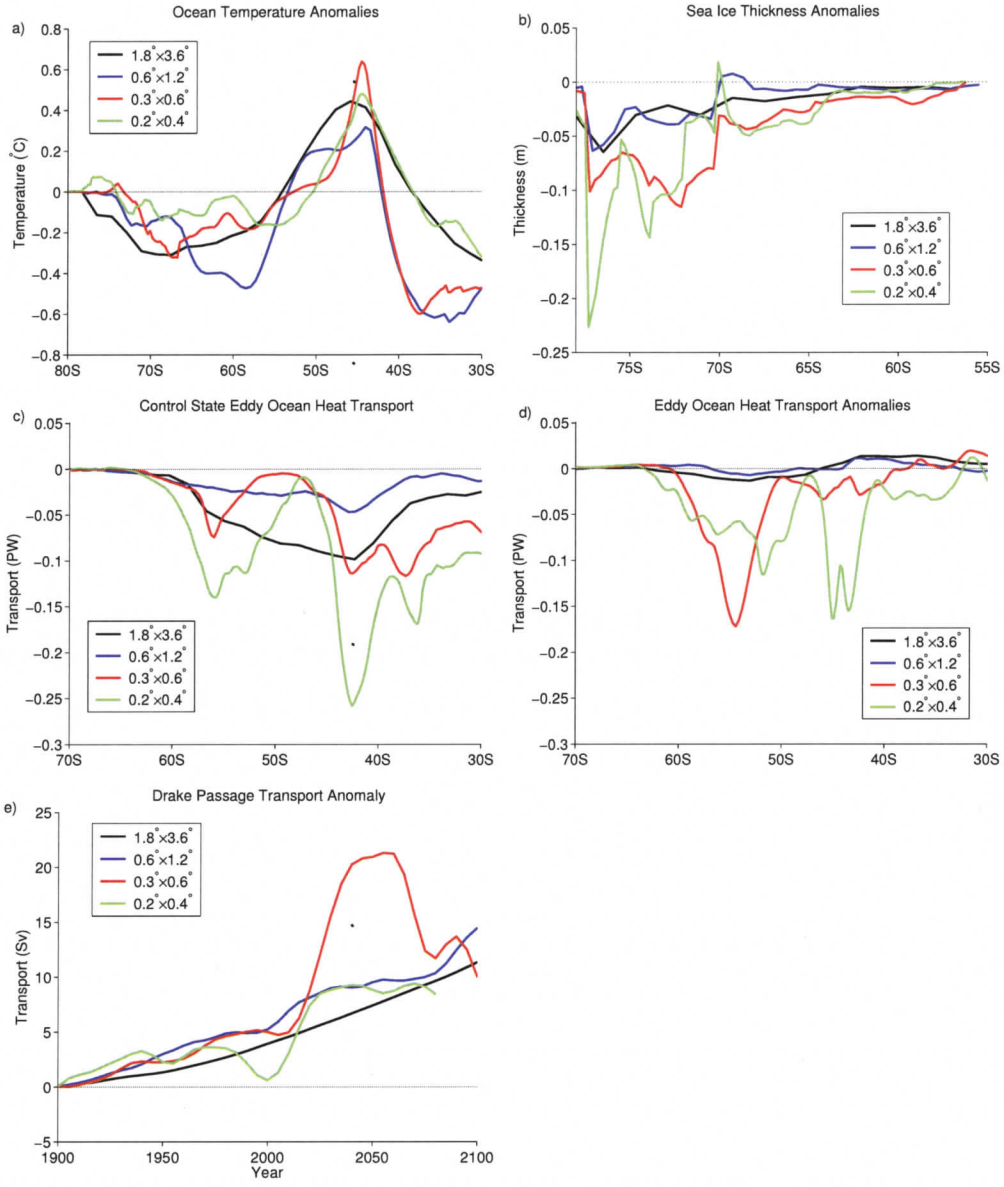

Figure 5.3: (a) Zonal average of ocean temperature anomalies from Fig. 5.1. (b) Zonal average sea ice thickness anomalies averaged over 2075-2080. (c) Zonal and depth integrated meridional ocean eddy heat transport in year 1900 and (d) anomalies in year 2080. Resolved eddy heat transports are shown at $0.3° \times 0.6°$ and $0.2° \times 0.4°$. GM90 parametrized eddy heat transports are shown at $1.8° \times 3.6°$ and $0.6° \times 1.2°$. (e) Change in the annual-mean transport through Drake Passage (calculated at 5 year intervals, and temporally smoothed).

(primed values refer to the eddy components and the overbar denotes temporal averaging), from instantaneous values of meridional velocity ($\mathbf{v}$) and potential temperature (θ) recorded at 5 day intervals. Parametrized eddy heat transports were calculated from annual averaged θ and the meridional bolus velocities produced by GM90. It is important to note that the resolved eddy heat transport of the two coarsest simulations and the GM90 induced heat transport of the two highest resolution models are not shown because in each case they remain less than 0.025 PW. The southward parametrized eddy heat transport of the two coarsest resolution simulations are found to be fairly uniformly distributed between 40-60°S. In contrast, resolved eddy transport in the two highest resolution simulations are patchy with larger transports identified over specific topographic features, particularly the Crozet plateau (near 43°S), and the Kerguelen and Campbell plateaus (near 55°S). The $0.2°\times0.4°$ resolved eddy heat transport compares well with those of the $0.25°\times0.25°$ model of *Jayne and Marotzke* (2002). Figure 5.3d similarly shows the resolved and parametrized eddy meridional heat transport anomalies in the year 2080. In response to the forcing, the GM90 parametrization induces very little change in heat transport, while resolved eddies exhibit a large increase in southward transport that can account for some of the reduction in high latitude cooling and greater loss of sea ice thickness found at eddy-permitting resolutions.

Observational estimates of the volume transport through Drake Passage are about 135 Sv. The control simulations have Drake Passage transports ranging from 115 Sv to 210 Sv (Table 5.1). This mismatch between observed and modelled values is not surprising, as only 3 of 18 WCRP CMIP3 models produce transports within 20% of the highly uncertain observations (*Russell et al.* 2006). Sea surface height and bottom pressure observations since the early 1980s show that ACC transport is positively correlated with SAM variability (*Hughes et al.* 2003, *Meredith et al.* 2004). This positive correlation is reproduced at a decadal scale by the simulations, with

ACC transport increasing as the westerly winds intensify and shift poleward. This intensification in transport occurs in all experiments and there is no indication that the ACC is at (or is reaching) an eddy saturated state in the higher resolution simulations (Fig. 5.3e). In an eddy-saturated regime changes in the wind stress induce changes in the intensity of the eddy field, which act to transport momentum vertically until it is taken up by bottom pressure torque, effectively dissapating the surface wind stress anomalies without influencing zonal transport (*Karsten et al.* 2002, *Meredith and Hogg* 2006). Achieving an eddy saturated state in these simulations seems unlikely given the relatively low eddy kinetic energies they exhibit, even at the highest resolution. An interesting feature of increasing resolution on the ACC transport response is an increase in the transport anomaly variability at eddy-permitting resolutions. The relatively large increase in transport between years 2025-2075 in the $0.3° \times 0.6°$ simulation results from weak decadal variability in the two forcing scenarios being out of 180° phase over a portion of that time period. Consequently, when the simulation forced with CO_2 and wind anomalies is differenced from the simulation forced with CO_2 alone a large transport anomaly results.

5.4 Conclusions

The zonal mean structure of the Southern Ocean temperature response to poleward intensifying winds through the 21^{st} century, with warming between 40-55°S and cooling at higher and lower latitudes, remains robust as model resolution increases. However, as expected, the response to wind anomalies has more regional structure at higher resolution. This is particularly evident in the warming of the Atlantic and Indian basins, where results show that the southward migration of better resolved fronts is associated with a strong local intensification of the temperature response, in agreement with the observations of *Gille* (2008). The parametrization of mesoscale eddies at coarse resolution is found to induce little change in heat transport, while re-

solved eddies exhibit a significant increase in southward transport. Consequently, at eddy-permitting resolutions there is a reduction in the zonal mean cooling response, and a greater loss of sea ice thickness south of about 55°S. All four models exhibit an increase in ACC transport, with more variability in the transport response at higher resolution. There is no indication of ACC eddy saturation in these simulations and no tendency toward saturation is observed as resolution increases.

Chapter 6

Conclusions

This dissertation explores the sensitivity of global climate simulations to an increase of horizontal resolution into the ocean eddy-permitting range. Four versions of the same global climate model, with horizontal resolutions ranging from $1.8°\times3.6°$ to $0.2°\times0.4°$, are employed to evaluate differences in the control states and the climate responses to various forcing scenarios. These simulation have aimed to contribute to the scientific understanding of ocean volume transport, ocean heat transport, water mass formation, and sea ice distribution.

Chapter 3 evaluates the effect of increasing horizontal resolution on the climate of the northern hemisphere Atlantic Ocean. In the pre-industrial control state, the representation of western boundary currents and meridional heat transport are improved with increasing resolution. Freshwater forcings similar to the final drainage of proglacial lakes Agassiz and Ojibway were applied evenly over the Labrador Sea and exclusively along the western boundary. The duration and maximum amplitude of Atlantic meridional overturning circulation response to the forcing showed little sensitivity to increasing resolution. An evaluation of the forcing impact on different regions of NADW formation with tracers reveals an increase in Labrador Sea deep convection at higher resolution likely mitigates the influence of better resolved boundary currents. With increasing resolution there is less cooling in the subpolar

west Atlantic, more cooling in the subpolar east Atlantic, and greater variability in the deep ocean response to the boundary forcing. While differences exist, the coarse resolution model response remains robust at finer horizontal resolutions. A caveat to these results is the exclusion of higher resolution bathymetry data in these simulations.

Chapter 4 evaluates the resolution dependence of the Southern Ocean meridional overturning circulation. At coarse resolutions North Atlantic deepwater tends to upwell diabatically at low-latitudes, so that the Southern Ocean is weakly coupled with the rest of the ocean. As resolution increases and eddy effects become less parametrized the interior circulation becomes more adiabatic and deep water increasingly upwells by flowing along isopycnals in the Southern Ocean, despite each model having the same vertical diffusivity profile. Separating the overturning circulation into mean and eddy-induced components demonstrates that both the permitted and the parametrized eddies induce overturning cells in the Southern Ocean with mass fluxes across mean isopycnals. It is found that for some density classes the transformation rate derived from surface buoyancy fluxes can provide a proxy for the net meridional transport in the upper Southern Ocean. Changes in the Southern Ocean overturning in response to poleward intensifying southern hemisphere winds concomitant with increasing atmospheric CO_2 through the 21st century are also investigated. Results suggest that the circulation associated with the formation of Antarctic Intermediate Water is likely to strengthen, or stay essentially unchanged, rather than to slow down.

Chapter 5 evaluates the resolution dependence of the Southern Ocean temperature and ACC response to poleward intensifying winds through the 20^{th} and 21^{st} centuries. Results show that the migration of distinct ocean fronts at higher resolutions, particularly along the northern edge of the ACC, is associated with a strong local intensification of the temperature response. There is also less high latitude cooling and

a greater loss of sea ice thickness at eddy-permitting resolutions, in conjunction with a significant increase in southward ocean eddy heat transport. All simulations show poleward migration of the ACC in the Atlantic and the western half of the Indian basin, while only slight changes are found in the eastern Indian and Pacific basins. There is no evidence in these simulations of the ACC reaching an eddy saturated state with ACC transport increasing at both coarse and eddy-permitting resolutions.

The refinement of grid resolution ideally allows GCMs to more explicitly manifest the dynamics of the climate system by reducing the dependence on sub-grid scale parametrizations, but there will always be potentially important dynamical degrees of freedom that remain unresolved. Consequently, numerically simulating the large space-time scales of the climate system is dependent on the accurate representation of phenomena that are resolved and the ability to parametrize important phenomena that are not resolved. 'How much resolution is enough?' is a key question that can only be answered with a keen understanding of the scientific question being asked. While this dissertation has pushed the use of coupled climate models into unprecedented computational territory, I believe even higher resolution (i.e $< 1/10°$) is required to accurately represent the effects of resolved mesoscale dynamics at high latitudes.

Taken together, this dissertation emphasizes the need for persistent evaluations of the delicate balance between resolved and parametrized physics in GCMs. This point is particularly accentuated by the resolution sensitivity of parametrized ocean convection, interior ocean diapycnal flows and parametrized versus resolved ocean heat transports. Furthermore, as simulated ocean flows tend to become more advectively dominant at higher resolution, the need to patiently tune model parameters becomes increasingly important. Tuning model parameters is a nontrivial task that becomes very cumbersome at high resolutions. However, improvements in the quality of climate simulations can be realized at higher resolution only if the tuning process

is carefully undertaken.

Finally, this dissertation clearly reveals many important questions requiring further research. How does increasing vertical resolution effect diapycnal ocean flows? What influence does the resolution of bathymetry have on North Atlantic convection and the MOC response to freshwater forcing? What effects would a more dynamical representation of atmospheric winds have? Will ACC transport saturation be found in models that more accurately represent the eddy kinetic energy of the Southern Ocean? Are mesoscale eddy resolving models needed to properly represent the ocean's role in climate or will a parametrization scheme suffice? It may be at least another decade before ocean eddy-resolving models can be routinely used for global climate modelling purposes on decadal or longer timescales. The examination of the effectiveness of parametrization schemes and model resolution must continue to be a priority.

Appendix A

Reynolds Number and Computational Modes

Following *Bryan et al.* (1975), this section describes the ocean resolution criteria employed for determining the coefficient of Laplacian lateral viscosity, A_M. The no-slip condition at side walls necessitates that a viscous boundary layer be resolved. Failure to resolve the viscous boundary layer may excite an erroneous computational mode that can extend into the ocean interior and is usually characterized by a checkerboard pattern in velocity fields. For grid spacings, Δ, greater than 100 km (i.e. coarse resolution models) the relevant resolution criterion for A_M is given by the Munk viscous boundary layer requirement,

$$A_M > \beta(\Delta\sqrt{3}/\pi)^3, \tag{A.1}$$

where $\beta = df/dy$. However, at grid spacing less than 100 km another criterion arises when centered differencing is used in a finite difference model. The associated computational mode can be excited if the Reynolds number is not less than a critical value. To illustrate the relation between the Reynolds number and the computational

mode consider the simplest case of the steady-state form of Burger's equation,

$$U\frac{\partial \rho}{\partial x} - A_M \frac{\partial^2 \rho}{\partial x^2} = 0. \tag{A.2}$$

If the derivatives are expressed as centered differences,

$$(R-2)\rho_{j+1} + 4\rho_j - (R+2)\rho_{j-1} = 0, \tag{A.3}$$

where $R = U\Delta/A_M$ is the Reynolds grid number. The general solution may be written as

$$\rho_j = C_1 + C_2\xi^j. \tag{A.4}$$

Substituting Eq. A.4 into Eq. A.3 gives

$$(R-2)\xi^2 + 4\xi - (R-2) = 0. \tag{A.5}$$

The two roots of Eq. A.5 are

$$\xi = 1,\ \xi = (2+R)/(2-R). \tag{A.6}$$

A computational mode arises when ξ is negative, since ξ^j alternates sign at adjacent grid points. The condition that ξ is positive definite is that $R = U\Delta/A_M < 2$. Consequently, for $\Delta = 44500\ m$ (i.e. the equatorial zonal grid spacing in a $0.2°\times0.4°$ degree grid), and $U = 1\ m/s$, a value of $A_M < 22250\ m^2/s$ has the potential to excite an erroneous computational mode.

Appendix B

Diapycnal Transformation

Following *Garrett et al.* (1995), consider the control volume between the sea surface and a control surface C, and between isopycnals with buoyancy b and $b+\delta b$ (Fig. 9). Let $\Psi(b)$ represents the volume flux across the isopycnal b between the surface and C. The net diffusive buoyancy flux is denoted by D. Then, assuming steady state, the conservation of the control volume gives

$$\Psi(b) - \Psi(b+\delta b) - (-\frac{d\Psi}{db})\delta b = 0, \tag{B.1}$$

whereas the conservation of buoyancy implies

$$\Psi(b)b - \Psi(b+\delta b)(b+\delta b) - (-\frac{d\Psi}{db})b\delta b + B_o\delta y + D(b) - D(b+\delta b) = 0, \tag{B.2}$$

where B_o is the buoyancy flux at the surface (positive downward). Dividing the latter equation by δb and taking the limit $\delta b \rightarrow 0$, gives:

$$\Psi(b) = B_o(dy/db) - dD/db \tag{B.3}$$

Thus, if the control surface bounding the isopycnals at depth is taken as the base of a well mixed surface layer and if the diapycnal diffusive flux in this layer is weak,

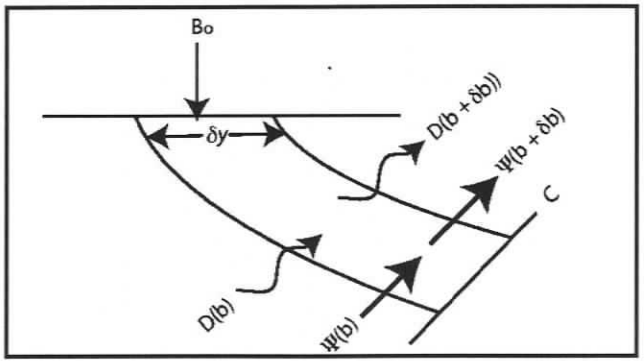

Figure B.1: Schematic of diapycnal transfer motion between two outcropping isopycnals bounded at depth by a control surface (C) arising from advective (Ψ), diffusive (D) and surface buoyancy (Bo) fluxes (adapted from *Garrett et al.* (1995)).

then the diapycnal volume flux within the layer can be estimated from the flux of buoyancy at the surface.

Bibliography

Alley, R., and A. Agustsdottir (2005), The 8k event: cause and consequence of a major Holocene abrupt climate change, *Quaternary Science Reviews*, *24*(10), 1123–1149.

Aoki, S., M. Yoritaka, and A. Masuyama (2003), Multidecadal warming of subsurface temperature in the Indian sector of the Southern Ocean, *Journal of Geophysical Research*, *108*(C4), 8081.

Barber, D., et al. (1999), Forcing of the cold event of 8,200 years ago by catastrophic drainage of Laurentide lakes, *Nature*, *400*(6742), 344–348.

Bauer, E., A. Ganopolski, and M. Montoya (2004), Simulation of the cold climate event 8200 years ago by meltwater outburst from Lake Agassiz, *Paleoceanography*, *19*(3), 3014–3027.

Beckmann, A., C. Boning, C. Koberle, and J. Willebrand (1994), Effects of increased horizontal resolution in a simulation of the North Atlantic Ocean, *Journal of Physical Oceanography*, *24*(2), 326–344.

Belkin, I., and A. Gordon (1996), Southern Ocean fronts from the Greenwich meridian to Tasmania, *Journal of Geophysical Research*, *101*(C2), 3675–3696.

Bond, G., W. Broecker, S. Johnsen, J. McManus, L. Labeyrie, J. Jouzel, and G. Bonani (1993), Correlations between climate records from North Atlantic sediments and Greenland ice, *Nature*, *365*(6442), 143–147.

Bond, G., et al. (1997), A pervasive millennial-scale cycle in North Atlantic Holocene and glacial climates, *Science*, *278*(5341), 1257–1266.

Böning, C., F. Bryan, W. Holland, and R. Doscher (1996), Deep-water formation and meridional overturning in a high-resolution model of the North Atlantic, *Journal of Physical Oceanography*, *26*(7), 1142–1164.

Böning, C., A. Dipert, M. Visbeck, S. Rintoul, and F. Scharzkopf (2008), The response of the Antarctic Circumpolar Current to recent climate change, *Nature Geoscience*, *1*(12), 864–869.

Broecker, W. S. (1991), The great ocean conveyor, *Oceanography*, *4*(2), 79–89.

Bryan, F., and R. Smith (1998), Modelling the North Atlantic circulation: from eddy-resolving to eddy-permitting, *International WOCE Newsletter*, *33*, 12–14.

Bryan, F., C. Boning, and W. Holland (1995), On the midlatitude circulation in a high-resolution model of the North Atlantic, *Journal of Physical Oceanography*, *25*(3), 289–305.

Bryan, K. (1991), Poleward heat transport in the Ocean, *Tellus*, *43AB*(4), 104–115.

Bryan, K., and L. Lewis (1979), Water mass model of the world ocean, *Journal of Geophysical Research*, *84*(NC5), 2503–2517.

Bryan, K., S. Manabe, and C. Pacanowski (1975), A global ocean-atmosphere climate model. Part II. The oceanic circulation, *Journal of Physical Oceanography*, *5*, 30–46.

Canuto, V., A. Howard, P. Hogan, Y. Cheng, M. Dubovikov, and L.Montenegro (2004), Modeling ocean deep convection, *Ocean Modelling*, *2*(1), 75–95.

Ciasto, L., and D. Thompson (2008), Observations of large-scale ocean-atmosphere interaction in the southern hemisphere, *Journal of Climate*, *21*(6), 1244–1259.

Clarke, G., D. L. J. Teller, and A. Dyke (2003), Superlakes, megafloods, and abrupt climate change, *Science*, *301*(5635), 922–923.

Danabasoglu, G., J. McWIlliams, and P. Gent (1994), The role of mesoscale tracer transport in the global circulation, *Science*, *264*(2), 1123–1126.

Danabasoglu, G., R. Ferrari, and J. McWilliams (2008), Sensitivity of an ocean general circulation model to a parameterization of near-surface eddy fluxes, *Journal of Climate*, *21*(6), 1192–1208.

Delworth., T., and F. Zeng (2008), Simulated impact of altered southern hemisphere winds on the Atlantic Meridional Overturning Circulation, *Geophysical Research Letters*, *35*(20), L20,708.

Dickson, R., and J. Brown (1994), The production of North Atlantic Deep Water: Sources, rates, and pathways, *Journal of Geophysical Research*, *24*(5162), 429–442.

Döös, K., and D. Webb (1994), The Deacon cell and other meridional cells of the Southern Ocean, *Journal of Physical Oceanography*, *416*(6883), 832–837.

Döös, K., J. Nycander, and A. Coward (2008), Lagrangian decomposition of the Deacon cell, *Journal of Geophysical Research*, *113*(C7), C07,028.

Döös, K., J. Nycander, and A. Coward (2009), Bolus decomposition of the Deacon cell, *in preparation*.

Drijfhout, S. (2005), What sets the surface eddy mass flux in the Southern Ocean?, *Journal of Physical Oceanography*, *35*(11), 2152–2166.

Ducet, N., P. L. Traon, and G. Reverdin (2000), Global high-resolution mapping of ocean circulation from TOPEX/Poseidon and ERS-1 and -2, *105*(19), 477–498.

Duffy, P., M. Wickett, and K. Caldeira (2002), Effect of horizontal grid resolution on the near-equilibrium solution of a global ocean-sea ice model, *Journal of Geophysical Research*, *107*(C7), 12.1–12.11.

Dukowicz, J., and R. Smith (1994), Implicit free-surface method for the bryan-cox-semtner ocean model, *Journal of Geophysical Research*, *99*(C4), 7991–8014.

Fanning, A. F., and A. J. Weaver (1996), An atmospheric energy moisture-balance model: climatology, interpentadal climate change and coupling to an OGCM, *Journal of Geophysical Research*, *101*(15), 15,111–15,128.

Fanning, A. F., and A. J. Weaver (1997), A horizontal resolution and parameter sensitivity study of heat transport in an idealized coupled climate model, *Journal of Climate*, *10*(10), 2469–2478.

Fanning, A. F., and A. J. Weaver (1998), Thermohaline variability: The effects of horizontal resolution and diffussion, *Journal of Climate*, *11*(4), 709–715.

Flatau, M., L. Talley, and P. Niiler (2003), The North Atlantic Oscillation, surface current velocities and SST changes in the subpolar North Atlantic, *Journal of Climate*, *16*(14), 2355–2369.

Fyfe, J. (2006), Southern ocean warming due to human influence, *Geophysical Research Letters*, *33*(19), L19,701.

Fyfe, J., and O. Saenko (2006), Simulated changes in the extratropical southern hemisphere winds and currents, *Geophysical Research Letters*, *33*(6), L06,701.

Fyfe, J., O. Saenko, K. Zickfeld, M. Eby, and A. Weaver (2007), The role of poleward intensifying winds on Southern Ocean warming, *Journal of Climate*, *20*(21), 5391–5400.

Ganachaud, A., and C. Wunsch (2000), Improved estimates of global ocean circulation, heat transport and mixing from hydrographic data, *Nature*, *408*(6811), 453–457.

Ganachaud, A., and C. Wunsch (2003), Large-scale ocean heat and freshwater transports during the World Ocean Circulation Experiment, *Journal of Climate*, *16*(4), 696–705.

Garrett, C., K. Speer, and E. Tragou (1995), The relationship between water mass formation and the surface buoyancy flux, with application to phillips Red-Sea model, *Journal of Physical Oceanography*, *25*(7), 1696–1705.

Gent, P., and J. McWilliams (1990), Isopycnal mixing in ocean circulation models, *Journal of Physical Oceanography*, *20*(1), 150 – 155.

Gent, P., J. Willebrand, T. McDougall, and J. McWilliams (1995), Parameterizing eddy-induced trancer transport in ocean circulation models, *Journal of Physical Oceanography*, *25*(4), 463–474.

Gerdes, R., C. Köberle, and J. Willebrand (1991), The influence of numerical advection schemes on the results of ocean general circulation models, *Climate Dynamics*, *5*(4), 211–226.

Gille, S. (2002), Warming of the Southern Ocean since the 1950s, *Science*, *295*(5558), 1275–1277.

Gille, S. (2008), Decadal-scale temperature trends in the southern hemisphere ocean, *Journal of Climate*, *21*(18), 4749–4765.

Gillett, N., and D. Thompson (2003), Simulation of recent southern hemisphere climate change, *Science*, *302*(5643), 273–275.

Gnanadesikan, A. (1999), A simple predictive model for the structure of the oceanic pycnocline, *Science*, *283*(5410), 2077–2079.

Gnanadesikan, A., et al. (2006), GFDL's CM2 global coupled climate models. Part II: The baseline ocean simulation, *Journal of Climate*, *19*(5), 675–697.

Hall, M., and H. Byrden (1982), Direct estimates and mechanisms of ocean heat transport, *Deep Sea Research*, *29*(3), 339–359.

Hallberg, R., and A. Gnanadesikan (2001), An exploration of the role of transient eddies in determining the transport of a zonally re-entrant current, *Journal of Physical Oceanography*, *31*(11), 3312–3330.

Hallberg, R., and A. Gnanadesikan (2006), The role of eddies in determining the structure and response of the wind-driven southern hemisphere overturning: Results from the Modeling Eddies in the Southern Ocean (MESO) project, *Journal of Physical Oceanography*, *36*(12), 2232–2252.

Hartmann, D. (1994), *Global Physical Climatology*, Academic Press, New York.

Hibler, W. (1979), Dynamic thermodynamic sea ice model, *Journal of Physical Oceanography*, *9*(4), 815–846.

Hirst, A., and T. McDougall (1998), Meridional overturning and dianeutral transport in a z-coordinate ocean model including eddy-induced advection, *Journal of Physical Coeanography*, *28*(6), 1205–1224.

Hogg, A., M. Meredith, J. Blundell, and C. Wilson (2008), Eddy heat flux in the Southern Ocean: response to variable wind forcing, *Journal of Climate*, *21*(4), 608–620.

Hughes, C. (2000), A theoretical reason to expect inviscid western boundary currents in realistic oceans, *Ocean Modelling*, *2*(1), 73–83.

Hughes, C., and E. Ashe (2003), Eddy forcing of the mean flow in the Southern Ocean, *Journal of Geophysical Research*, *106*(C2), 2713–2722.

Hughes, C., P. Woodworth, M. Meredith, and V. Stepanov (2003), Coherence of Antarctic sea levels, Southern Hemishpere Annular Mode, and flow through Drake Passage, *Geophysical Research Letters*, *29*(20), 1950.

Hunke, E. C., and J. K. Dukowicz (1997), An elastic-viscous-plastic model for sea ice dynamics, *Journal of Physical Oceanography*, *27*(9), 1849–1867.

Iudicone, D., G. Madec, and T. McDougall (1997), Water-mass transformations in a neutral density framework and the key role of light penetration, *Journal of Physical Oceanography*, *38*(7), 1357–1376.

Jayne, S., and J. Marotzke (2002), The oceanic eddy heat transport, *Journal of Physical Oceanography*, *32*(12), 3328–3345.

Jochum, M., G. Danabasoglu, M. Holland, Y. Kwon, and W. Large (2008), Ocean viscosity and climate, *Journal of Geophysical Research*, *113*(C6), C06,017.

Johns, W., J. Bane, and D. Watts (1995), Gulf Stream structure, transport, and recirculation near 68W, *Journal of Geophysical Research*, *100*(C1), 817–838.

Johnson, H., and D. Marshall (2004), Global teleconnections of meridional overturning circulation anomalies, *Journal of Physical Oceanography*, *34*(7), 1702–1722.

Karsten, R., H. Jones, and J. Marshall (2002), The role of eddy transfer in setting the stratification and transport of ae circumpolar current, *Journal of Physical Oceanography*, *32*(1), 39–54.

Kistler, R., et al. (2001), The NCEP-NCAR 50-year reanalysis: Monthly means CD-ROM and documentation, *Bulletin of the American Meteorological Society*, *82*(2), 247–267.

Lavender, K., R. Davis, and W. Owens (2002), Observations of open-ocean deep convection in the Labrador Sea from subsurface floats, *Journal of Physical Oceanography*, *32*(2), 511–526.

Lee, M., A. Nurser, A. Coward, and B. de Cuevas (2007), Eddy advective and diffusive transports of heat and salt in the Southern Ocean, *Journal of Physical Oceanography*, *37*(5), 1376–1393.

Leverington, D., J. Mann, and J. Teller (2002), Changes in the bathymetry and volume of glacial Lake Agassiz between 9200 and 7700 C-14 yr BP, *Paleoceanography*, *18*(4), 16(1)–16(8).

Levitus, S., R. Burgett, and T. Boyer (1994), *World Ocean Atlas, Volumes 3 and 4*, NOAA, Dept. of Commerce, USA.

Levitus, S., J. Antonov, T. Boyer, and C. Stephens (2000), Warming of the world ocean, *Science*, *287*(5461), 2225–2229.

Lumpkin, R., and K. Speer (2003), Large-scale vertical and horizontal circulation in the North Atlantic Ocean, *Journal of Physical Oceanography*, *33*(9), 1902–1920.

Macdonald, A., and C. Wunsch (1996), An estimate of global ocean circulation and heat fluxes, *Nature*, *382*(6590), 436–439.

Manabe, S., and R. J. Stouffer (1995), Simulation of abrupt climate change induced by freshwater input to the North Atlantic Ocean, *Nature*, *378*(6553), 165–167.

Marshall, J., and F. Schott (1999), Open-ocean convection: Observations, theory and models, *Reviews of Geophysics*, *37*(1), 1–64.

Matthews, H., A. Weaver, M. Eby, and K. Meissner (2003), Radiative forcing of climate by historical land cover change, *Geophysical Research Letters*, *30*(2), 27(1)–27(4).

McAvaney, B., et al. (2001), Model evaluation, in IPCC Third Assesment Report.

McDougall, T., and P. McIntosh (1996), The temporal-residual-mean velocity. Part I: Derivation and the scalar conservation equations, *Journal of Physical Oceanography*, *26*(12), 2653–2665.

McIntosh, P., and T. McDougall (1996), Isopycnal averaging and the residual mean circulation, *Journal of Physical Oceanography*, *26*(8), 1655–1660.

Meissner, K., and P. Clark (2006), Impact of floods versus routing events on the thermohaline circulation, *Geophysical Research Letters*, *33*(15), L15,704.

Meissner, K. J., A. Schmittner, A. J. Weaver, and J. F. Adkins (2003), Ventilation of the North Atlantic Ocean during the Last Glacial Maximum: A comparison between simulated and observed radiocarbon ages, *Paleoceanography*, *18*(2), 1023.

Meredith, M., and A. Hogg (2006), Circumpolar response of Southern Ocean eddy activity to a change in the Southern Annular Mode, *Geophysical Research Letters*, *33*(16).

Meredith, M., P. Woodworth, C. Hughes, and V. Stepanov (2004), Changes in the ocean transport through Drake Passage during the 1980s and 1990s, forced by changes in the Southern Annular Mode, *Geophysical Research Letters*, *31*(21), L21,305.

Morrill, C., and M. Jacobsen (2005), How widespread were climate anomalies 8200 years ago?, *Geophysical Research Letters*, *32*(19), L19,701.

NGDC (2007), National Geophysical Data Center 5-minute gridded global relief data collection, *http://www.ngdc.noaa.gov/mgg/fliers/93mgg01.html*.

Oschlies, A. (2002), Improved representation of upper-ocean dynamics and mixed layer depths in a model of the North Atlantic on switching from eddy-permitting

to eddy resolving grid resolution, *Journal of Physical Oceanography*, *32*(8), 2277–2298.

Pacanowski, R. (1995), *MOM 2 Documentation User's Guide and Reference Manual, GFDL Ocean Group Technical Report*, NOAA/GFDL, Princeton.

Pacanowski, R., and S. Griffies (2000), *MOM 3 Documentation User's Guide and Reference Manual, GFDL Ocean Group Technical Report*, NOAA/GFDL, Princeton.

Peixoto, J., and A. Oort (1993), *Physics of Climate*, American Institute of Physics, New York.

Polzin, K., J. Toole, and R. Schmitt (1997), Finescale parameterizations of turbulent dissipation, *Journal of Physical Oceanography*, *25*(2), 306–328.

Radko, T., and J. Marshall (2004), Eddy-induced diapycnal fluxes and their role in the maintenance of the thermocline, *Journal of Physical Oceanography*, *34*(2), 372–383.

Rahmstorf, S. (2002), Ocean circulation and climate during the past 120,000 years, *Nature*, *419*(6903), 207–214.

Randall, D., et al. (2007), Climate Models and their Evaluation, in: Climate Change 2007: The Physical Science Basis. Intergovernmental Panel on Climate Change Fourth Assesment Report.

Renssen, H., H. Goosse, T. Fichefet, and J. Campin (2001), The 8.2 kyr BP event simulated by a global atmosphere-sea ice-ocean model, *Geophysical Research Letters*, *28*(8), 1567–1570.

Renssen, H., H. Goosse, and T. Fichefet (2002), Modeling the effect of freshwater

pulses on the early Holocene climate: The influence of high frequency climate variability, *Paleoceanography*, *17*(2), 10.1–10.15.

Roberts, J., et al. (2004), Impact of an eddy-permitting ocean resolution on control and climate change simulations with a global coupled GCM, *Journal of Climate*, *17*(1), 372–382.

Russell, J., R. Stouffer, and K. Dixon (2006), Intercomparison of the Southern Ocean circulations in IPCC coupled model control simulations, *Journal of Climate*, *19*(18), 4560–4575.

Saenko, O. (2007b), Projected strengthening of the Southern Ocean winds: some implications for the deep ocean circulation, *Ocean Circulation: Mechanisms and Impacts. AGU Geophysical Monograph Series*, *173*(1365-382).

Saenko, O., J. Fyfe, and M. England (2005), On the response of the oceanic wind-driven circulation to atmospheric CO_2 increase, *Climate Dynamics*, *25*(4), 415–426.

Saenko, O., A. Weaver, D. Robitaille, and G. Flato (2007a), Warming of the subpolar Atlantic triggered by freshwater discharge at the continental boundary, *Geophysical Research Letters*, *34*(15).

Sallee, J., K. Speer, and R. Morrow (2008), Response of the Antarctic Circumpolar Current to atmospheric variability, *Journal of Climate*, *21*(12), 3020–3039.

Screen, J., N. Gillett, D. Stevens, G. Marshall, and H. Roscoe (2008), The role of eddies in the Southern Ocean temperature response to the Southern Annular Mode, *Journal of Climate*, *21*, in press.

Semtner, A., and R. Chervin (1988), A simulation of the global ocean circulation with resolved eddies, *Journal of Geophysical Research*, *93*(C12), 15,502–15,522.

Sen Gupta, A., and M. England (2006), Coupled ocean-atmosphere-ice response to variations in the Southern Annular Mode, *Journal of Climate*, *19*(18), 4457–4486.

Sloyan, B., and S. Rintoul (2001), The Southern Ocean limb of the global deep overturning circulation, *Journal of Physical Oceanography*, *31*(1), 143–173.

Smethie, W., and R. Fine (2001), Rates of North Atlantic Deep Water formation calculated from chlorofluorocarbon inventories, *Deep-Sea Research*, *48*(1), 189–215.

Smith, R., M. Maltrud, F. Bryan, and M. Hecht (2000), Numerical simulation of the North Atlantic at 1/10 degrees, *Journal of Physical Oceanography*, *30*(7), 1532–1561.

Speer, K., E. Guilyardi, and G. Madec (2000a), Southern Ocean transformation in a coupled model with and without eddy mass fluxes, *Telus*, *52*(5), 554–565.

Speer, K., S. Rintoul, and B. Sloyan (2000b), The diabatic Deacon cell, *Journal of Physical Oceanography*, *30*(12), 3212–3222.

Stammer, D. (1997), Global characteristics of ocean variability from regional TOPEX/POSEIDON altimeter measurements, *Journal of Physical Oceanography*, *28*, 1743–1769.

Stocker, T. (1998), Climate change - The seesaw effect, *Science*, *282*(5386), 61–62.

Stommel, H. (1961), Thermohaline convection with two stable regimes of flow, *Tellus*, *13*, 224–230.

Stouffer, R., et al. (2006), Investigating the causes of the response of the thermohaline circulation to past and future climate changes, *Journal of Climate*, *19*(8), 1365–1387.

Talley, L. (2003), Shallow, intermediate, and deep overturning components of the global heat budget, *Journal of Physical Oceanography*, *33*(3), 530–560.

Talley, L., J. Reid, and P. Robbins (2003), Data-based meridional overturning streamfunctions for the global ocean, *Journal of Climate*, *16*(19), 3213–3226.

The FRAM Group (D. Webb et al.) (1991), An eddy-resolving model of the Southern Ocean, *EOS, Transactions of the American Geophysical Union*, *72*(15), 169–174.

Thompson, D., and S. Solomon (2002), Interpretation of recent southern hemisphere climate change, *Science*, *296*(5569), 895–899.

Toggweiler, J., and J. Russell (2008), Ocean circulation in a warming climate, *Nature*, *451*(7176), 286–288.

Treguier, A., S. Theetten, E. Chassignet, T. Penduff, R. Smith, L. Talley, J. Beismann, and C. Boning (2005), The North Atlantic subpolar gyre in four high-resolution models, *Journal of Physical Oceanography*, *14*(7), 757–774.

Treguier, A., M. England, S. R. ad G. Madec, J. L. Sommer, and J. Molines (2007), Southern Ocean overturning across streamlines in an eddying simulation of the Antarctic Circumpolar Current, *Ocean Science*, *3*, 491–507.

von Grafenstein, U., H. Erlenkeuser, J. Muller, J. Jouzel, and S. Johnsen (1998), The cold event 8200 years ago documented in oxygen isotope records of precipitation in Europe and Greenland, *Climate Dynamics*, *14*(2), 73–81.

Walin, G. (1982), On the relationship between sea surface heat flow and thermal circulation in the ocean, *Tellius*, *34*(2), 187–195.

Wang, Y., and L. Mysak (2005), Response of the ocean climate and terrestrial carbon cycle to Holocenc freshwater discharge after 8 kyr BP, *Geophysical Research Letters*, *32*(15), 14,241–14,259.

Weaver, A. J., and T. M. Hughes (1992), Stability and variability of the thermohaline circulation and its link to climate, *Trends in Physical Oceanography, Research Trends Series, Council of Scientific Research Integration, Trivandrum, India*, *1*(1), 15–70.

Weaver, A. J., et al. (2001), The UVic Earth System Climate Model: Model description, climatology, and applications to past, present and future climates, *Atmosphere-Ocean*, *39*(4), 361–428.

Wiebe, E., and A. Weaver (1999), On the sensitivity of global warming experiments to the parameterization of sub-grid scale ocean mixing, *Climate Dynamics*, *15*(12), 875–893.

Willebrand, J., B. Barnier, C. Boning, C. Dieterich, P. Killworth, C. L. Provost, Y. Jia, J. Molines, and A. New (2001), Circulation characteristics in three eddy permitting models of the North Atlantic, *Progress in Oceanography*, *48*, 123–161.

Wood, R., A. Keen, J. Mitchell, and J. Gregory (1999), Changing spatial structure of the thermohaline circulation in response to atmospheric co_2 forcing in a climate model, *Nature*, *399*(6736), 572–575.

Wunsch, C. (1999), Where do ocean eddy fluxes matter?, *Journal of Geophysical Research*, *104*(C6), 13,235–13,249.

Wunsch, C. (2006), *Past and Future Changes of the Meridional Overturning Circulation: Mechanisms and Impact*, AGU monograph, U.S.A.

Wunsch, C. (2007), The past and future ocean circulation from a contemporary perspective, *Ocean Circulation: Mechanisms and Impacts.AGU Geophysical Monograph Series*, *173*, 53–74.

Zickfeld, K., J. Fyfe, O. Saenko, M. Eby, and A. Weaver (2007), Response of the global carbon cycle to human-induced changes in southern hemisphere winds, *Geophysical Research Letters*, *34*(12), L12,712.